Convective aggregation in realistic convective-scale simulations

AGU PUBLICATIONS

Journal of Advances in Modeling Earth Systems

RESEARCH ARTICLE
10.1002/2017MS000980

Convective aggregation in realistic convective-scale simulations

Christopher E. Holloway[1]

[1]Department of Meteorology, University of Reading, Reading, UK

Key Points:
- Convective self-aggregation in the Unified Model is driven mainly by direct radiative feedbacks
- Low-level circulations also aid aggregation, but are not primarily forced by radiation anomalies
- Convective aggregation occurs at SSTs as low as 290 K, mainly due to cloud-radiation feedbacks

Supporting Information:
- Supporting Information S1
- Movie S1
- Movie S2
- Movie S3
- Movie S4
- Movie S5

Correspondence to:
C. E. Holloway,
c.e.holloway@reading.ac.uk

Citation:
Holloway, C. E. (2017), Convective aggregation in realistic convective-scale simulations, *J. Adv. Model. Earth Syst.*, *09*, doi:10.1002/2017MS000980.

Received 17 MAR 2017
Accepted 17 MAY 2017
Accepted article online 22 MAY 2017

Abstract To investigate the real-world relevance of idealized-model convective self-aggregation, five 15 day cases of real organized convection in the tropics are simulated. These include multiple simulations of each case to test sensitivities of the convective organization and mean states to interactive radiation, interactive surface fluxes, and evaporation of rain. These simulations are compared to self-aggregation seen in the same model configured to run in idealized radiative-convective equilibrium. Analysis of the budget of the spatial variance of column-integrated frozen moist static energy shows that control runs have significant positive contributions to organization from radiation and negative contributions from surface fluxes and transport, similar to idealized runs once they become aggregated. Despite identical lateral boundary conditions for all experiments in each case, systematic differences in mean column water vapor (CWV), CWV distribution shape, and CWV autocorrelation length scale are found between the different sensitivity runs, particularly for those without interactive radiation, showing that there are at least some similarities in sensitivities to these feedbacks in both idealized and realistic simulations (although the organization of precipitation shows less sensitivity to interactive radiation). The magnitudes and signs of these systematic differences are consistent with a rough equilibrium between (1) equalization due to advection from the lateral boundaries and (2) disaggregation due to the absence of interactive radiation, implying disaggregation rates comparable to those in idealized runs with aggregated initial conditions and noninteractive radiation. This points to a plausible similarity in the way that radiation feedbacks maintain aggregated convection in both idealized simulations and the real world.

Plain Language Summary Understanding the processes that lead to the organization of tropical rainstorms is an important challenge for weather forecasters and climate scientists. Over the last 20 years, idealized models of the tropical atmosphere have shown that tropical rainstorms can spontaneously clump together. These studies have linked this spontaneous organization to processes related to the interaction between the rainstorms, atmospheric water vapor, clouds, radiation, surface evaporation, and circulations. The present study shows that there are some similarities in how organization of rainfall in more realistic computer model simulations interacts with these processes (particularly radiation). This provides some evidence that the work in the idealized model studies is relevant to the organization of tropical rainstorms in the real world.

1. Introduction

A number of studies have shown that self-aggregation in idealized radiative-convective equilibrium (RCE) simulations is linked to feedbacks between convection, moisture, clouds, radiation, and surface fluxes [e.g., *Tompkins*, 2001; *Bretherton et al*., 2005; *Muller and Held*, 2012; *Wing and Emanuel*, 2014; *Coppin and Bony*, 2015; *Muller and Bony*, 2015; *Wing and Cronin*, 2016; *Holloway and Woolnough*, 2016]. A review of convective self-aggregation in idealized simulations is presented in *Wing et al*. [2017].

A key question about these idealized studies is the extent to which self-aggregation processes are relevant to organized convection in nature. Several studies have found that satellite observations comparing snapshots of different levels of convective organization with similar large-scale forcing show decreased mean column water vapor (CWV) and increased outgoing longwave radiation (OLR) in agreement with idealized studies of self-aggregation [*Tobin et al*., 2012, 2013; *Stein et al*., 2017].

Part of the debate over the relevance of self-aggregation to real-world convection centers on the degree to which cloud-system resolving models (CRMs) or global climate models (GCMs) adequately represent

convective processes and convective organization. However, another part of this debate involves the degree to which idealized model configurations are representative of the real world. It is this second question that the present paper investigates. Some modeling studies have increased the complexity of idealized configurations to address this question, though still in an idealized framework, and the results largely support a connection between their simulated convective organization processes and those in more idealized self-aggregation simulations. For instance, using a constant nonzero Coriolis parameter in idealized RCE generally leads to spontaneous tropical cyclogenesis [e.g., *Bretherton et al*., 2005; *Nolan et al*., 2007; *Wing et al*., 2016]. *Arnold and Randall* [2015] found that global superparameterized simulations with uniform SST and Earth-like rotation can lead to behavior similar to the Madden-Julian Oscillation (MJO), with cloud-radiation feedbacks making large contributions to growth of organized convection. *Bretherton and Khairoutdinov* [2015] showed that near-global-scale explicit convection simulations with Earth-like rotation and latitudinally varying SSTs exhibited growth rates of moisture anomalies similar to those in more idealized self-aggregation, and they again noted that radiation feedbacks play a key role. On the other hand, studies of idealized nonrotating RCE coupled to a slab ocean have found that air-sea coupling can delay or even prevent self-aggregation depending on the experiment setup [*Bretherton et al*., 2005; *Reed et al*., 2015; *Hohenegger and Stevens*, 2016].

In the present study, aggregation processes in realistic atmosphere-only model simulations of real case studies of organized convection are compared to idealized self-aggregation simulations in the same model from *Holloway and Woolnough* [2016, hereinafter HW16]. Using idealized simulations of RCE at 4 km grid spacing and 576 km $\times$ 576 km domain size with periodic lateral boundaries, HW16 found that self-aggregation in the control run was largely initiated and maintained by the direct radiative effect based on analysis of the budget of the spatial variance of column-integrated frozen moist static energy (MSE) following *Wing and Emanuel* [2014]. Mechanism denial experiments in HW16 showed that interactive radiation (as opposed to fixed prescribed radiative temperature increments) was necessary for strong self-aggregation to occur (except in an experiment in which rain evaporation was also suppressed to prevent cold pools); the suppression of interactive radiation also caused the disaggregation of convection in runs initialized with an aggregated state. Turning off interactive surface sensible and latent heat fluxes (by prescribing fixed uniform surface fluxes) also prevented self-aggregation in HW16, although when constant prescribed surface fluxes were increased to slightly higher values self-aggregation did occur; interactive surface fluxes were not necessary to maintain self-aggregation. Suppressing rain evaporation in HW16 led to even faster self-aggregation, supporting findings by *Jeevanjee and Romps* [2013] that cold pools forced by rain evaporation inhibit or slow self-aggregation.

In the present study, the same model used in HW16 is run in limited-area configuration for five 15 day case studies of real organized tropical convection, with lateral boundary conditions and SSTs taken from operational analyses. For each case, most of the same mechanism-denial experiments performed in HW16 are also conducted. Analysis of the budget of the spatial variance of MSE is also performed in order to compare influences of aggregation processes in these realistic cases to those of the idealized simulations in HW16.

This paper is organized as follows. Data sources are given in section 2, model configuration and experiment setup are explained in section 3, and a few details about methodology are outlined in section 4. The control simulations for each case are presented, compared to observations, and analyzed with respect to the budget of the spatial variance of MSE in section 5. Section 6 presents analysis of the mechanism-denial experiments and the implied sensitivity of convective aggregation and mean state to interactive radiation, interactive surface fluxes, and rain evaporation. Finally, a discussion of results and the study's conclusions are presented in section 7.

2. Data

The satellite brightness temperature data, SST data, and atmospheric pressure-level data used to identify the five case studies are discussed in *Stein et al*. [2017, section 2]. Precipitation observations are taken from the 3 hourly 0.25° merged Tropical Rainfall Measurement Mission (TRMM) 3B42 product [*Huffman et al*., 2007], which combines mostly microwave satellite retrievals with brightness temperature data to cover spatial gaps. European Centre for Medium-Range Weather Forecasts (ECMWF) operational analyses, which are at approximately 25 km grid spacing in the tropics and archived for the Year of Tropical

Convection (YOTC, May 2008 to April 2010) [*Waliser et al*., 2012], are used to compare to model simulations and also as lateral boundary conditions for the limited-area model runs.

3. Model Configuration and Experiment Design

The limited-area setup of version 7.5 of the Met Office Unified Model (UM) [*Davies et al*., 2005], which is semi-Lagrangian and nonhydrostatic, is used for the runs in this study. The model itself, which is nearly the same as that used in the idealized runs in HW16, is described in the next two paragraphs, with the details of the limited-area domain and experimental design discussed in the final paragraph of this section.

As in HW16, 4 km horizontal grid spacing with 70 vertical levels is used, and vertical spacing between levels ranges from tens of meters in the boundary layer to around 250 m in the lower free troposphere to 1 km near the tropopause. Also as in HW16, the time step is 30 s, the model top is at 40 km, and there is a sponge layer in the upper few levels.

The model physics settings are similar to those described for the "4-km 3Dsmag" model version in *Holloway et al*. [2013] and to those in the idealized simulations in HW16. This model version includes Smagorinsky-type subgrid mixing in the horizontal and vertical dimensions (with no local or nonlocal boundary layer scheme). The single-moment mixed-phase microphysics scheme has three components: ice/snow, cloud liquid water, and rain [*Wilson and Ballard*, 1999]. The model uses a CAPE-limited version of the convective parameterization that asymptotes to a 30 min CAPE time scale at zero CAPE but has a CAPE time scale that rapidly increases with increasing CAPE such that for typical tropical CAPE values and in all the simulations in this study, virtually all rainfall is generated explicitly rather than by the parameterization [*Roberts*, 2003; *Lean et al*., 2008]. As mentioned in *Holloway et al*. [2013], the parameterization is on mainly to slightly increase numerical stability and generate shallow convection in conditions without mean ascent.

There are some differences from the idealized setup in HW16, described below. There is a normal diurnal cycle of solar insolation based on the dates and locations of the cases. SSTs come from the European Centre for Medium-Range Weather Forecasts (ECMWF) operational analysis at the initial time (with full spatial variability) but are then held constant in time. Atmospheric fields are initialized from the ECWMF analysis at the initial time, and lateral boundaries are nudged toward a slightly-larger-domain 12 km model with parameterized convection. The 12 km model has the same initial conditions, and its lateral boundaries are nudged toward ECMWF analyses which are updated every 6 h; this one-way nesting methodology is the same as that used in *Holloway et al*. [2013]. (Note that the lateral boundary conditions are the same for all mechanism-denial experiments for a given case, so this constrains the degree to which these experiments can differ from the control run). The Coriolis parameter depends on the actual latitude at each grid point. The domain of each case is centered on the equator and approximately $20^\circ \times 20^\circ$ latitude/longitude. Four of the five cases contain a small amount of land, and this land has interactive soil moisture and soil temperature as well as prescribed vegetation. Because the surface land temperature is interactive, the interactive radiation scheme is used over land points for all experiments, even those in which the atmospheric radiation increments are prescribed over ocean points. Moisture conservation is not enforced by a Priestley scheme (which was used in HW16) because that scheme was not compatible with nonperiodic lateral boundaries, but nonconservation of moisture is minimized by a Met Office branch of code that accounts for negative advective increments of ice and liquid by the semi-Lagrangian advection scheme and balances these with appropriate changes to local water vapor and thermal energy. This conserves moisture to within about 0.3 mm d^{-1}, or about 3–4% of the average rainfall rate. A Charnock relationship is used to calculate surface roughness lengths interactively, and there is no prescribed minimum wind speed.

4. Methods

Here I provide a few details about methodology, although most discussion of methods is presented in the relevant results sections. The five 15 day cases were chosen based on observational analyses of $10^\circ \times 10^\circ$ boxes analyzed at 3 hourly intervals from July 2006 to April 2011 as described in *Stein et al*. [2017]. The specific objective criteria were (1) the box was either in the Indian or Pacific basins (sea fraction $\geq$0.95); (2) the box was centered on the equator (to minimize Coriolis effects); (3) the dates fell in the YOTC period (May 2008 to April 2010); (4) the Simple Convective Aggregation Index (SCAI) [*Tobin et al*., 2012] was finite and

less than 0.5 (but with cold cloud area $\geq$0.01) for at least 5 days; (5) precipitation $\geq$3 mm d^{-1}; and (6) mean SST $\geq$26°C. The last three conditions were allowed to have gaps of up to 12 h during the 5 day period for which they did not have to be satisfied; multiple gaps up to this length were allowed, although in practice most fields satisfy the criteria all the time, with SCAI showing the largest frequency of gaps. The 15 day case was then defined to start 5 days before the start of the 5 day period, and the total domain of the simulations were the 20° × 20° domains centered on the original boxes.

There were 164 such events between 30°S and 30°N (ignoring condition 2 above), but only 16 were centered on the equator and thus satisfied condition 2. Of these 16, two were quite far west (centered on 60°E), nine were quite far east (east of 180°E), and the other five were the ones actually chosen here, since they were more obviously in or near the "warm pool" region. The warm pool region was favored here because it was assumed to be most similar to typical RCE configurations used in self-aggregation studies, and because it is the main MJO region. The entire selection process above occurred before the cases were explored further with observations, and before any simulations were run, to maintain objectivity as much as possible.

Although the intention was originally to study aggregation within the inner 10° × 10° domain for each case, this ended up resulting in artificial differences in convective aggregation metrics and the mean state between experiments depending on the exact positioning of large-scale features within the larger domain and how much they happened to overlap with the inner averaging domain. Therefore, for the rest of the paper unless otherwise noted, analysis is performed over the whole 20° × 20° box rather than using the 10° × 10° inner boxes to select the cases originally.

SCAIP, a precipitation-based version of SCAI used as an aggregation metric for simulations and TRMM rainfall in this study, is defined in the same way as SCAI in *Tobin et al*. [2012], with $\mathrm{SCAIP} = (N/\mathrm{Nmax}) \times (D_0/L) \times 1000$, where N is the number of clusters, Nmax is the number of pixels in the domain divided by 2, D_0 is the geometric mean distance between all pairs of clusters, and L is the length of the domain. SCAIP is calculated by first coarse-graining the precipitation to a 24 km grid, similar to the 25 km grid for TRMM. The precipitation clusters are found using a threshold of 0.0062 mm h^{-1} for both the models and for TRMM; this is derived by multiplying 0.00159 (based on maintaining roughly equal convective region area fractions at the original 4 km grid scale as a similar method using brightness temperature methods in the same models) times 39.0625, which is the number of 4 km boxes in one 25 km box. The threshold is equal to 1.49 mm d^{-1} which is not far above the minimum value (1 mm d^{-1}) that is reliably observable by TRMM [*Huffman et al*., 2007]. Lower values of SCAIP correspond to larger amounts of organization, at least for a given mean rain rate.

5. Characteristics of Aggregation in Control Runs

As discussed in section 4, the five cases were objectively selected based on criteria related to large-scale conditions and aggregation state in the inner domain, although results are presented for the full 20° × 20° domain. Table 1 shows the longitude range, dates, and mean SST for each case (the latitude range is 10°S–10°N for all cases). Note that the first two cases overlap in space and time (they both follow the evolution of an active MJO event moving from within the domain to the east), but they should be independent enough in terms of initial conditions and boundary conditions that they can be treated as independent cases (or at least as substantially different "ensemble members" of a partly shared case). The first three cases contain a small amount of land (Sri Lanka and the southern tip of India) and the fourth case contains New Britain and the Solomon Islands, which are an even smaller fraction of the domain. The fifth case contains no land in the simulations.

Table 1. Longitude and Date Ranges, and Mean SST, for Each Case[a]

Longitude Range	Date Range	Mean SST (K)
65°E–85°E	25 Jan 2009 to 8 Feb 2009	301.6
70°E–90°E	31 Jan 2009 to 14 Feb 2009	301.6
75°E–95°E	4 Apr 2010 to 18 Apr 2010	303.0
150°E–170°E	19 Nov 2008 to 3 Dec 2008	302.3
165°E–185°E	2 May 2009 to 16 May 2009	302.1

[a]Latitude range is 10°S–10°N for all cases.

5.1. Comparison With Observations

Figures 1a–1d show the overall evolution and temporal means of CWV, CWV IQR (Interquartile Range), CWV UQR (the "Upper-quantile Range", which is the 95th percentile minus the median), and the CWV autocorrelation length scale (smallest spatial lag at which the spatial autocorrelation drops below e^{-1}, averaged for

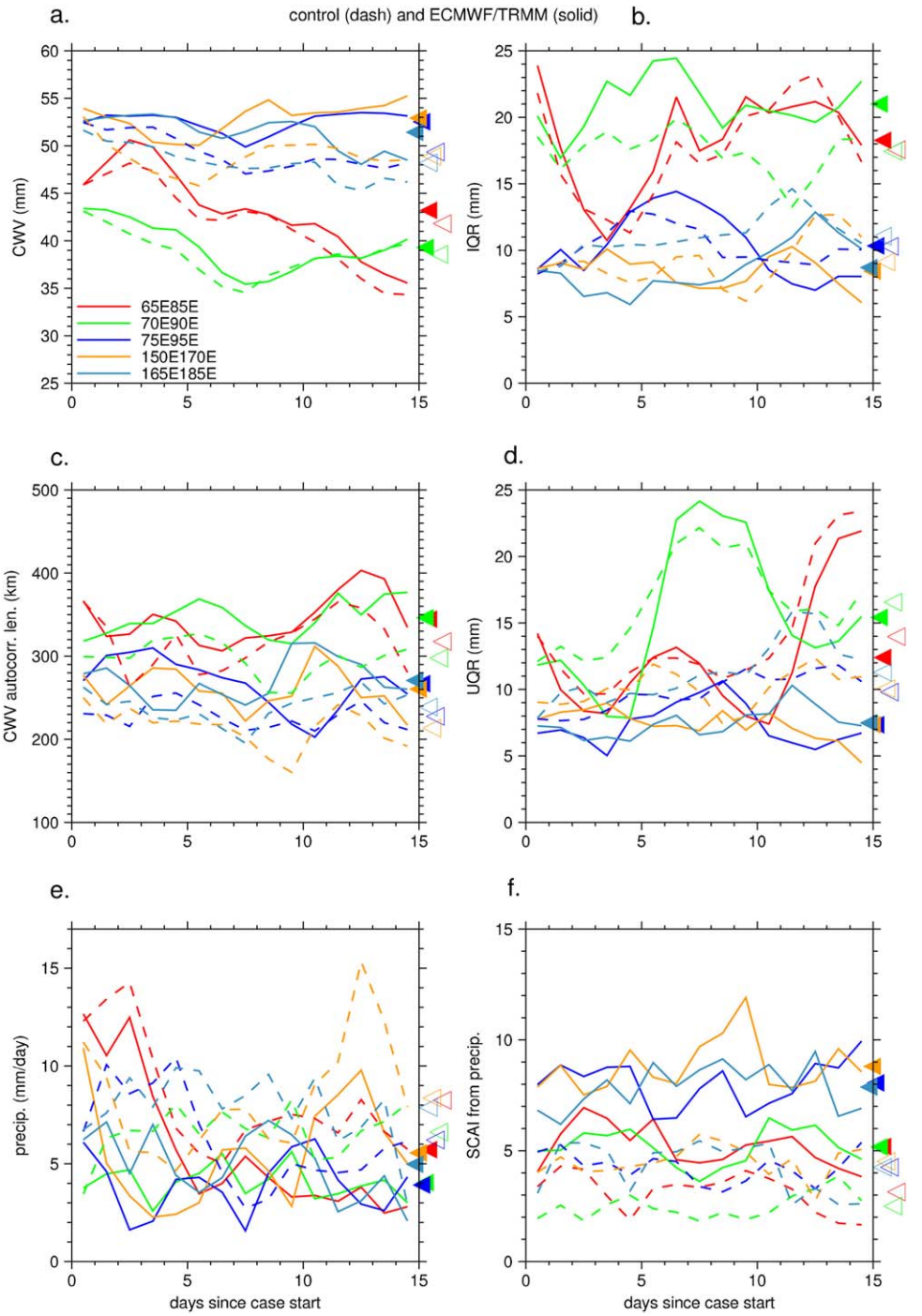

Figure 1. (a) Mean CWV for control run (dash) and ECMWF (solid) for case, (b) as in Figure 1a but for CWV IQR, (c) as in Figure 1a but for CWV UQR, (d) as in Figure 1a but for CWV autocorrelation length scale, (e) mean precipitation for control run (dash) and TRMM (solid) for each case, (f) SCAIP for control run (dash) and TRMM (solid) for each case. Time-means shown by triangles at right for each figure, with filled triangles for ECMWF/TRMM and open triangles for control runs.

all rows and columns) for all five control simulations (dashed lines and open triangles) and ECMWF analyses (solid lines and filled triangles). These figures give a sense of the range and variability of both model control runs and observations among the five cases, and can be compared to similar figures in HW16. The mean biases will be explored further in later sections, but in most cases the models follow the main variability of the observations. IQR and UQR represent the spread in the CWV distribution, and larger values correspond

to larger amounts of organization or aggregation; however, the two indices disagree with each other on the overall evolution of aggregation over time, especially for the two Indian Ocean cases that are furthest west (65°E–85°E and 70°E–90°E). Those two Indian Ocean cases that are furthest west (and that overlap in space and time) have the lowest mean CWV and the most organized values of aggregation metrics in general. The autocorrelation length scale is expected to be larger for more aggregated conditions because it signifies larger moist and dry regions.

Figures 1e and 1f show mean rainfall and SCAIP compared with TRMM. SCAIP is used instead of SCAI (which uses brightness temperature to define clusters) because these runs will be compared later to runs without interactive radiation (see section 4 for details on SCAIP methodology). (Although brightness temperature can be computed from runs even if they do not have interactive radiation, in practice SCAI is sensitive to upper level cloud temperature variability which is reduced by suppressing interactive radiation, so SCAI is not a good way to compare convective aggregation between runs with and without interactive radiation.) The mean modeled rainfall does not agree with TRMM as much as CWV agrees with ECMWF (partly because the boundary conditions from ECMWF may not be completely consistent with TRMM rainfall anyway). There is also a wet bias for rainfall in the model which is common for this kind of explicit convection limited-area simulation; this is discussed for *Cascade* simulations of the Indo-Pacific Warm Pool in *Holloway et al*. [2012]. SCAIP is consistently lower (more organized) in the model runs than in TRMM observations, and the variability does not match very closely between models and observations, but these discrepancies might be the result of known limitations in the ability of explicit convection models at this grid spacing to simulate rainfall cluster sizes and correct frequencies of high rain rates [*Holloway et al*., 2012]. The time-mean SCAIP values are lower for the two westernmost cases than for the other three cases when comparing among only TRMM or only model values, consistent with these two cases being more aggregated in agreement with the other aggregation metrics—however, the day-to-day variability for the different cases is not very consistent with that seen in the other aggregation metrics, so SCAIP may not be a good indicator of that level of aggregation variability.

5.2. Moist Static Energy Variance Budget Analysis

As in HW16 and *Wing and Emanuel* [2014], the frozen moist static energy (MSE, or h) should be approximately conserved for moist adiabatic processes and is defined as,

$$h = c_p T + gz + L_v q_v - L_f q_i, \tag{1}$$

where c_p is the specific heat of dry air, T is the air temperature, g is gravitational acceleration, z is height above the surface, L_v is the latent heat of vaporization, q_v is the specific humidity with respect to water vapor, L_f is the latent heat of fusion, and q_i is the specific humidity with respect to ice condensates (including frozen precipitation).

For some quantity x, let $\{x\}$ be defined as the horizontal domain-mean of x and the anomaly from this mean is defined as x'. Also let $\hat{x} = \int_0^{z_{top}} x\rho dz$, where ρ is the density. Then, again following *Wing and Emanuel* [2014], the budget for the horizontal spatial variance of $\hat{h}$ is,

$$\frac{1}{2}\frac{\partial \hat{h}'^2}{\partial t} = \hat{h}'\mathrm{THF}' + \hat{h}'\mathrm{S\hat{W}}' + \hat{h}'\mathrm{L\hat{W}}' - \hat{h}'(\nabla_{\mathbf{h}} \cdot \hat{\mathbf{v}h})', \tag{2}$$

where THF is the total surface heat flux (latent plus sensible), SW and LW are the net shortwave and longwave heating, respectively, and $\nabla_{\mathbf{h}} \cdot \hat{\mathbf{v}h}$ is the horizontal divergence of the vertically integrated flux of h. The first three terms on the rhs of equation (2) are the spatial covariances between $\hat{h}$ and the three diabatic processes that can change $\hat{h}$. The last term, which represents the spatial covariance between $\hat{h}$ and transport processes or "convergence" of MSE, is calculated as a residual from the remaining budget as in *Wing and Emanuel* [2014] and HW16; the three diabatic terms are calculated from instantaneous hourly thermodynamic fields and hourly mean fluxes as in HW16. The covariance terms can be used to determine how much each process contributes to changes in the variance of $\hat{h}$ and thus to changes in aggregation (although, as with the IQR and UQR, there is no mathematically required relationship between the variance of $\hat{h}$ and the spatial scales of convective organization).

Figure 2 shows the evolution of $\{\hat{h}'^2\}$ for the five control runs. As seen in the IQR, UQR, autocorrelation length scale, and SCAIP in Figure 1, there are differences in aggregation state between cases, and the

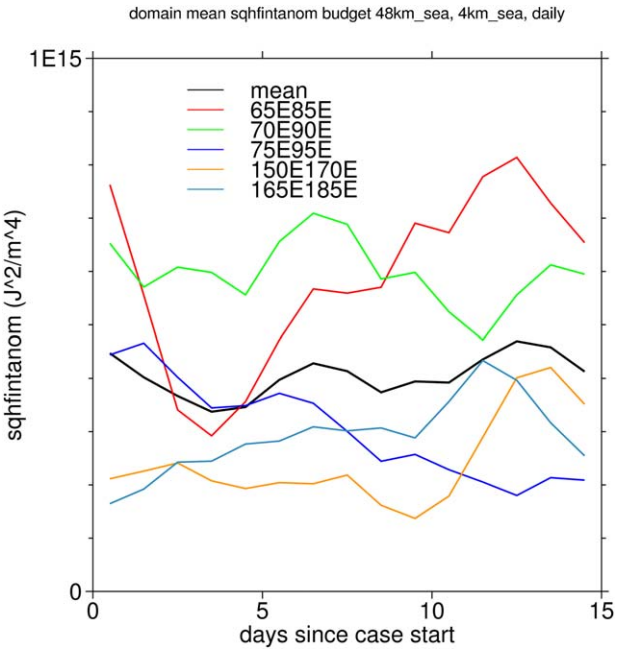

Figure 2. Domain-day mean $\{\hat{h}'^2\}$ ($J^2\ m^{-4}$) for control runs (sea points only) of each case.

different indices also disagree somewhat, but overall larger $\{\hat{h}'^2\}$ corresponds to more aggregated conditions as judged from the other indices and as seen in idealized self-aggregation studies (and there seems to be more agreement with IQR and autocorrelation length scale than with UQR or SCAIP). On the whole, Figure 2 shows that the two westernmost cases in the Indian Ocean are the most aggregated, with the other cases being less aggregated. The 65°E–85°E case becomes more aggregated over the last two thirds of the period, while the 75°E–95°E case becomes less aggregated. The mean of the five control runs is similar in magnitude to $\{\hat{h}'^2\}$ in the idealized control run from HW16 during the latter half of the period when the convection is aggregated (their Figure 9e), suggesting these realistic simulations have a comparable degree of aggregation to aggregated idealized simulations using this metric.

Figure 3 shows the domain-time mean of the terms in the $\{\hat{h}'^2\}$ budget. The radiation terms are positive, as in the idealized control run in HW16 once the convection has aggregated (their Figure 4b), and the order of magnitude of the terms is similar in both studies. However, the longwave term is at least twice as large as shortwave and sometimes even more than this in Figure 3, which is different from the mature stage of aggregation in HW16, in which the two terms are comparable to each other. (Note that the clear-sky fluxes were not output, so these cannot be used to infer cloud radiation effects as was done in HW16). The surface flux terms are negative but they show the largest spread between the different cases: for several cases the surface flux term is relatively small in magnitude while in the two westernmost Indian Ocean cases it is among the largest-magnitude terms. The two runs with the most negative surface flux term also have the lowest mean CWV (and column relative humidity [CRH], the CWV divided by the column-integrated saturation specific humidity, not shown) and the largest regions of low-CWV air, suggesting a strong negative surface flux feedback for aggregation in these regions (although the terms will also have larger magnitudes for these cases because they are more aggregated and thus the overall variance is larger); the other three cases have values that are roughly similar to those for the mature stage of aggregation

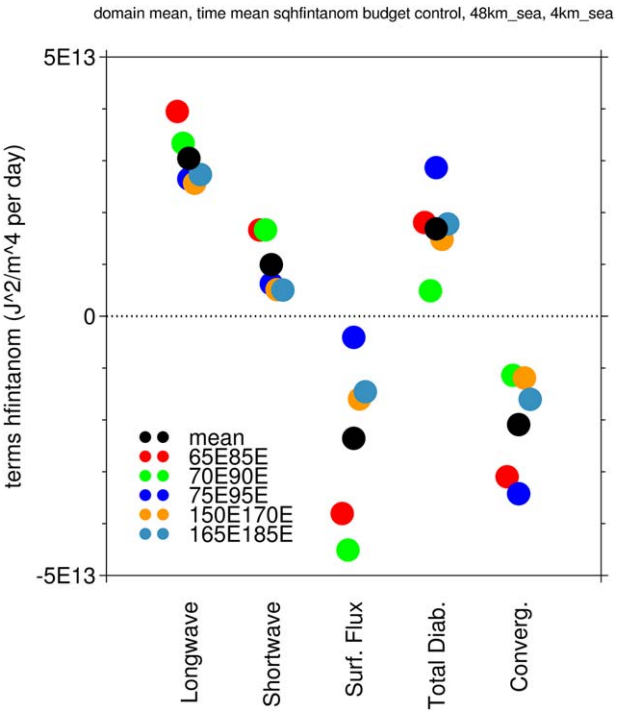

Figure 3. Daily mean values of domain-mean terms in the $\hat{h}'^2$ budget ($J^2\ m^{-4}\ d^{-1}$) for control runs (sea points only) of each case. Note that *x* axis positions for each term vary slightly across cases for graphical clarity.

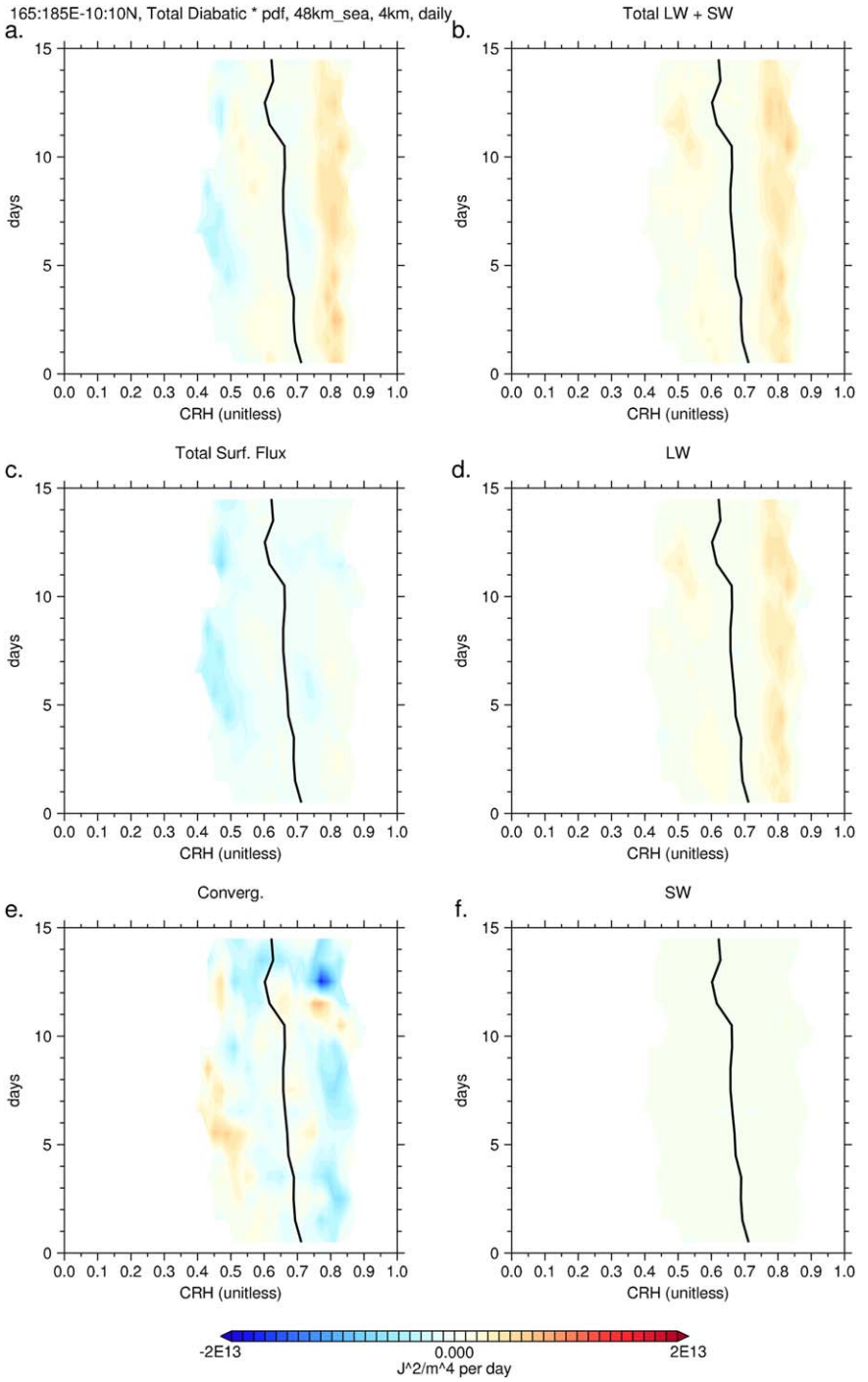

Figure 4. Daily mean values of 48 km × 48 km blocks for terms in the $\hat{h}'^2$ budget (sea points only) conditionally averaged by column relative humidity (CRH) for each day and multiplied by the probability density for that CRH and day, in units $J^2\ m^{-4}\ d^{-1}$. The figures show (a) the sum of all diabatic terms, (b) the sum of contributions from longwave and shortwave radiation, (c) surface heat flux, (d) longwave radiation, (e) horizontal convergence of h flux, and (f) shortwave radiation; for the control run from 165°E–185°E. The black line is the $\hat{h}' = 0$ contour.

in HW16. *Bretherton and Khairoutdinov* [2015] also found negative surface flux feedbacks, particularly due to strong surface fluxes in dry air intrusions, in their large channel simulations, and *Arnold and Randall* [2015] found negative surface flux feedbacks in both nonrotating and rotating global uniform-SST simulations for mature aggregation. The convergence term is negative, suggesting positive gross moist stability in the

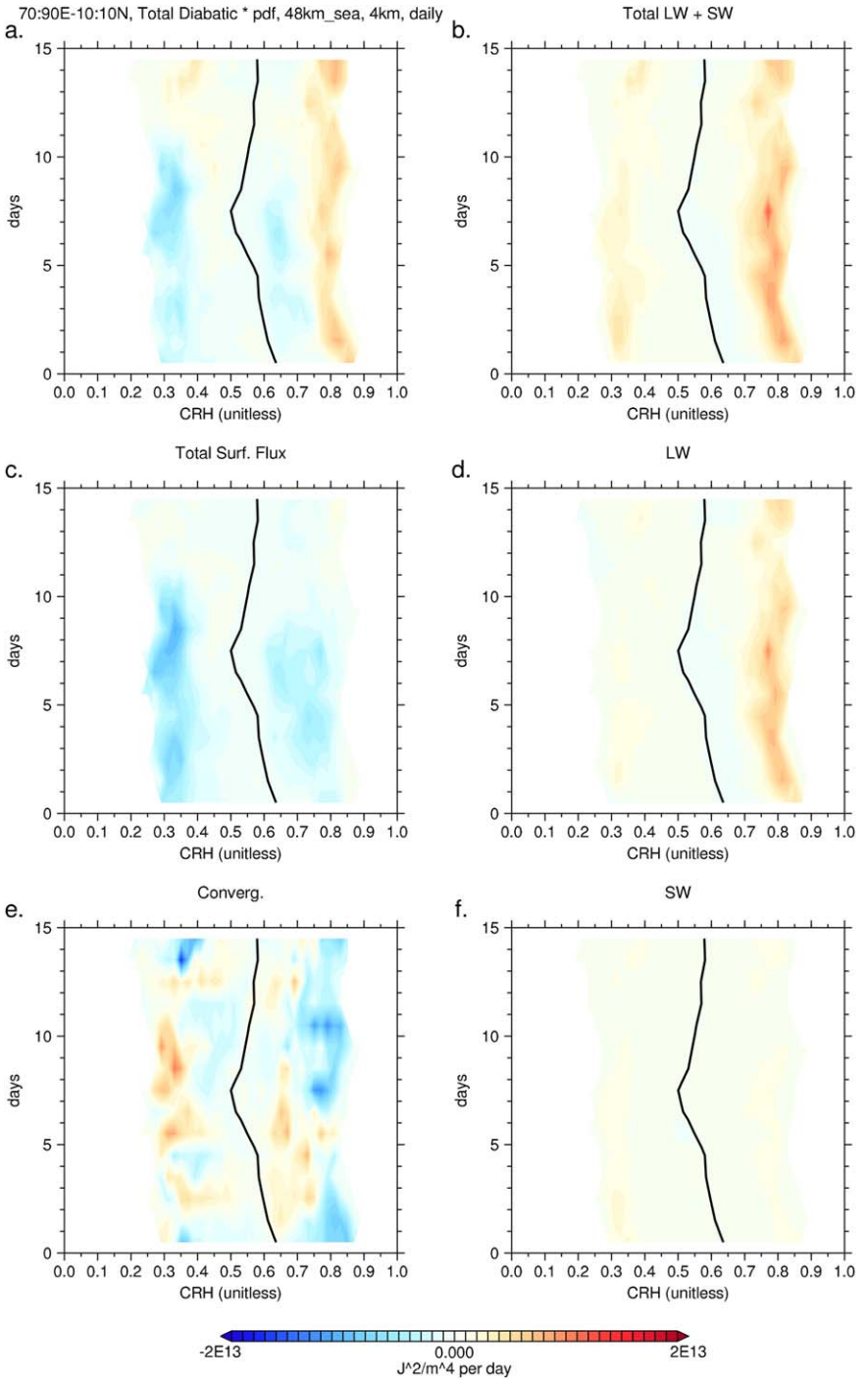

Figure 5. Daily mean values of 48 km × 48 km blocks for terms in the $\hat{h}\prime^2$ budget (sea points only) conditionally averaged by column relative humidity (CRH) for each day and multiplied by the probability density for that CRH and day, in units $J^2\ m^{-4}\ d^{-1}$. The figures show (a) the sum of all diabatic terms, (b) the sum of contributions from longwave and shortwave radiation, (c) surface heat flux, (d) longwave radiation, (e) horizontal convergence of h flux, and (f) shortwave radiation; for the control run from 70°E–90°E. The black line is the $\hat{h}\prime=0$ contour.

moist convective regions (or other disaggregating transport processes); these values are roughly consistent with the mature stage of aggregation in HW16. The total diabatic terms (the sum of longwave, shortwave, and surface flux terms) are positive and largely balance the negative convergence terms. Note that the convergence term includes both internal transport and transport from the lateral boundary conditions.

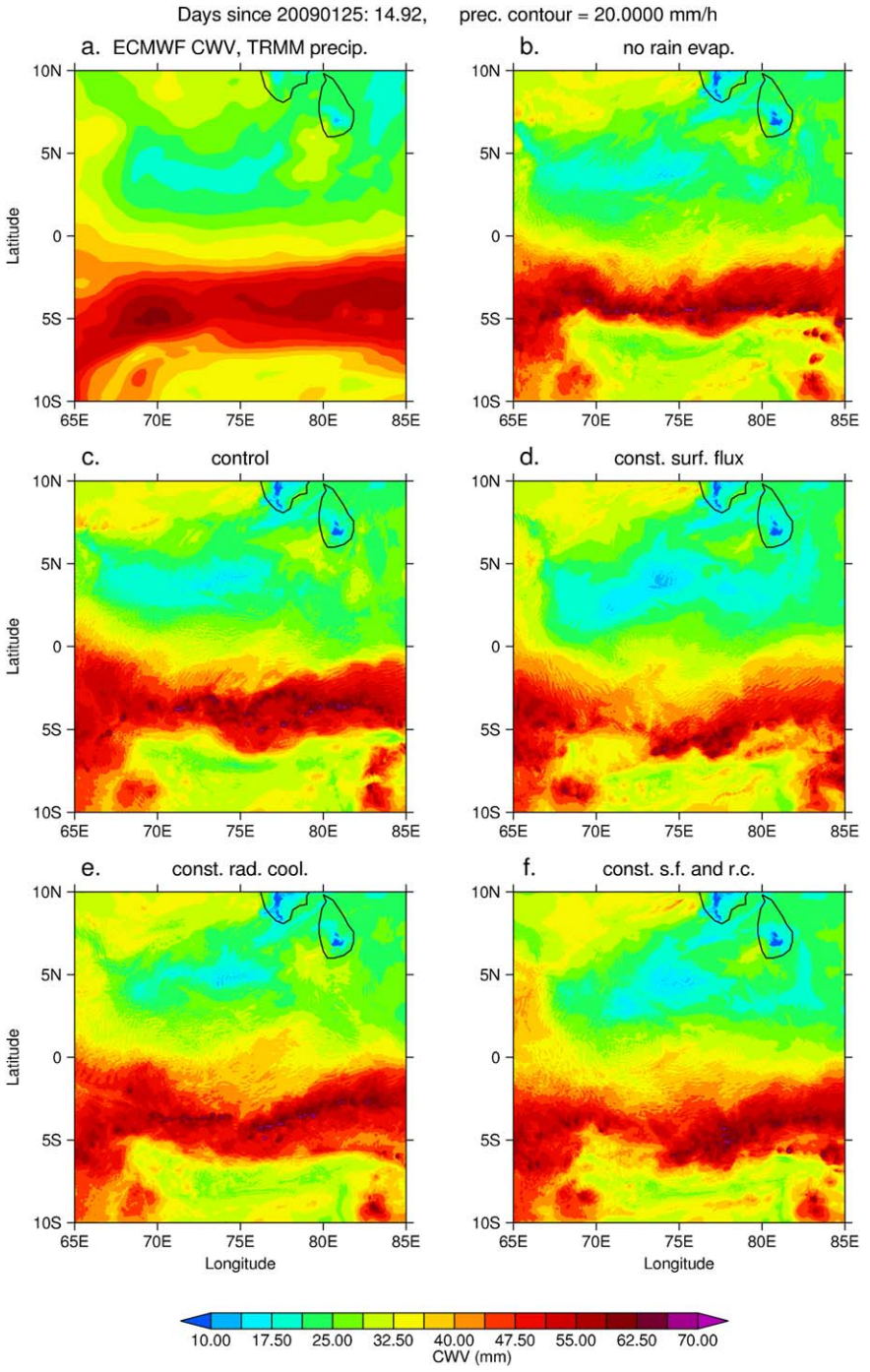

Figure 6. Snapshot of 65°E–85°E case at day 14.92 of the simulation (22 UTC on 8 February 2009) with CWV in color and the 20 mm h^{-1} precipitation contour in black for (a) ECMWF analysis (CWV) and TRMM (precipitation), (b) run with suppressed evaporation of rainfall, (c) control run, (d) run with fixed constant prescribed surface fluxes over sea, (e) run with fixed constant prescribed radiative cooling over sea, and (f) run with fixed constant prescribed surface fluxes and radiative cooling over sea. The fields are shown on their native grids (25 km for observations and 4 km for model runs).

As in HW16, the evolution of the $\{\hat{h}'^2\}$ budget terms is investigated by averaging each term in 48 km × 48 km blocks for each day and ranking them by CRH. Examples of contour plots of these daily block averages binned by CRH and multiplied by the fraction of total blocks in that bin for each day for two of the cases are shown in Figures 4 and 5. Analogous figures for the other three cases are shown in supporting information Figures S1–S3. Larger magnitudes indicate larger contributions to the budget, either because of

stronger average feedback or larger frequency of occurrence or both. In general for all cases, the longwave term is large mainly in high CRH bins, with smaller values of either sign in other bins. The shortwave term is positive but smaller than the longwave term, and it has peaks at either low or high bins. The large negative surface flux components come from both high and low CRH bins, but it is present at most times at the low CRH bins, representing a strong negative surface flux feedback for these regions as in HW16 (their Figure 6c). The convergence term is more variable, but there is a tendency for negative terms to be more likely at high CRH and positive at low CRH. This analysis confirms the importance of the longwave term in the moistest regions for maintenance of organized convection, as seen in HW16 (their Figure 6d).

6. Sensitivity to Fixed Surface Fluxes and Radiative Cooling, and to Nonevaporation of Rain

One of the main questions of this study is: How do mechanisms that are important for self-aggregation in idealized simulations affect convective organization and the mean state in realistic simulations? In this section, "mechanism-denial" experiments are analyzed and compared to similar experiments in HW16 and other idealized RCE studies. These experiments include simulations with prescribed constant radiative cooling, constant surface fluxes, and a combination of the two, as well as a simulation with suppressed evaporation of rainfall. (Note that, unlike in HW16, there is no experiment including both constant radiative cooling and suppressed rain evaporation, though this could be an idea for future work.)

While the experiments are similar to those in HW16, there are some important differences. For the experiments with constant radiative cooling, the values over sea have a single profile of radiation temperature increments for all locations and times, but any land regions still have fully interactive radiation to preserve surface temperature stability (see section 4 for details). The constant surface flux experiments also prescribe fixed values for the surface turbulent heat fluxes which are constant in space and time over sea points, while land points have an interactive surface as in the control runs. Also, because the control simulations here have SSTs that vary in space (though not in time), the potential *effect* of the constant surface flux experiments is much greater than in the idealized experiments in HW16 because, in addition to the interactive surface fluxes, horizontal variations in SST are effectively eliminated (except for very small differences in surface upward longwave radiation). This can have additional effects on the location and organization of convection that are not possible in the idealized experiments, which all have uniform SST.

6.1. Spatial Variability

An example snapshot of CWV and a contour of high precipitation for analyses/observations and the control and four experiments for a time near the end of the 65°E–85°E case is shown in Figure 6. Although the observations in Figure 6a are on a coarser grid (25 km) than the model runs (4 km), the large-scale organization appears to be well represented by all model runs, showing the importance of the lateral boundary conditions for maintaining these features. However, the positions of the main precipitation events vary slightly among the models. In addition to this, there are some systematic differences apparent in the experiments. For example, the driest oceanic region is even drier in the two experiments with constant surface fluxes (Figures 6d and 6f) than in their respective interactive surface flux runs (Figures 6c and 6e). This discrepancy appears to be due to drier-than-average specific humidity which leads to increased surface fluxes and slightly less dry conditions in the runs with interactive surface fluxes, at least for this case and region. The run with suppressed rain evaporation has more linear precipitation features and appears to be slightly more aggregated than the control. Comparing the two runs with constant radiative cooling (Figures 6e and 6f) with their respective interactive radiation runs (Figures 6c and 6d), the constant radiative cooling runs have smaller dry regions and larger moist regions on average, with somewhat weaker gradients in CWV.

The corresponding snapshot for the final hour of the 150°E–170°E case is shown in Figure 7. Here there is somewhat more disagreement between the model runs and observations in terms of the locations of the main precipitation regions and dry regions, and the dry CWV bias in all model runs is more apparent as well. However, because the moist, precipitating region is much larger than in the 65°E–85°E case, several "dry patches," which may be similar to those thought to begin the self-aggregation process in idealized models [e.g., *Wing and Emanuel*, 2014], can be seen in Figure 7 (e.g., around 166°E, 2.5°N). These patches tend to be slightly smaller and less dry in the two runs with constant radiative cooling (Figures 7e and 7f) than in their respective interactive radiation runs (Figures 7c and 7d). The precipitation fields

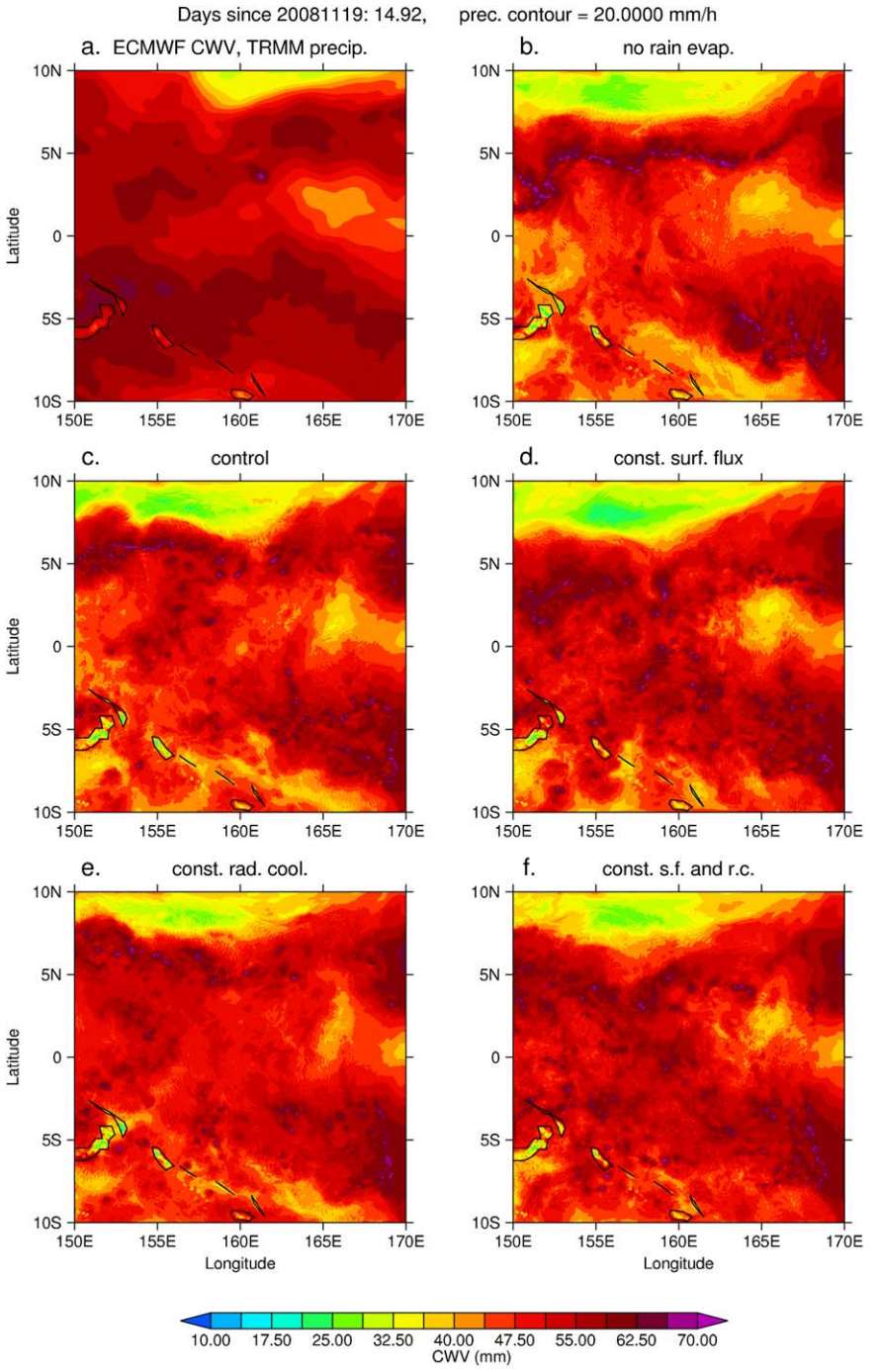

Figure 7. Snapshot of 150°E–170°E case at day 14.92 of the simulation (22 UTC on 3 December 2008) with CWV in color and the 20 mm h^{-1} precipitation contour in black for (a) ECMWF analysis (CWV) and TRMM (precipitation), (b) run with suppressed evaporation of rainfall, (c) control run, (d) run with fixed constant prescribed surface fluxes over sea, (e) run with fixed constant prescribed radiative cooling over sea, and (f) run with fixed constant prescribed surface fluxes and radiative cooling over sea. The fields are shown on their native grids (25 km for observations and 4 km for model runs).

are slightly different, but again there does not appear to be a systematic difference in the organization of precipitation due to interactive radiation. The run with suppressed rain evaporation (Figure 7b), however, shows much more linear, organized, and aggregated precipitation features than the other model runs. The effect of prescribing constant surface fluxes on CWV is that, again, the driest oceanic region is even drier in the two experiments with constant surface fluxes (Figures 7d and 7f), while the CWV in the

moister regions is somewhat higher, compared to their respective interactive surface flux runs (Figures 7c and 7e).

The corresponding images from the final hour of the other three cases are shown in supporting information Figures S4–S6. The main ideas above still hold in general. Animations of these fields for the five cases can also be found in the supporting information Movies S1–S5.

6.2. Aggregation Metrics and Mean State

Figure 8a shows CWV biases for each model experiment relative to ECMWF (for sea points only) averaged for the five cases, showing that all of the experiments develop a case-mean dry CWV bias of ∼2 mm within the first 2 days, as shown in Figure 1a for the control runs. This dry CWV bias is also consistent with the tendency for a dry bias in the *Cascade* runs [*Holloway et al*., 2013, 2015] that used a fairly similar model version (but which did not have the additional code used here to minimize nonconservation of moisture in the advection scheme). The case-averaged differences between each experiment and the control run (Figure 8b) show that there is also a tendency for the constant radiative cooling experiments to have larger mean CWV than the control experiments, while the no-rain-evaporation experiments tend to have lower mean CWV on average and the constant surface flux experiments (with interactive radiation) show little average difference. The systematic differences attributable to constant radiative cooling are of the same sign as the corresponding CWV differences between the equilibrium states of analogous experiments in idealized

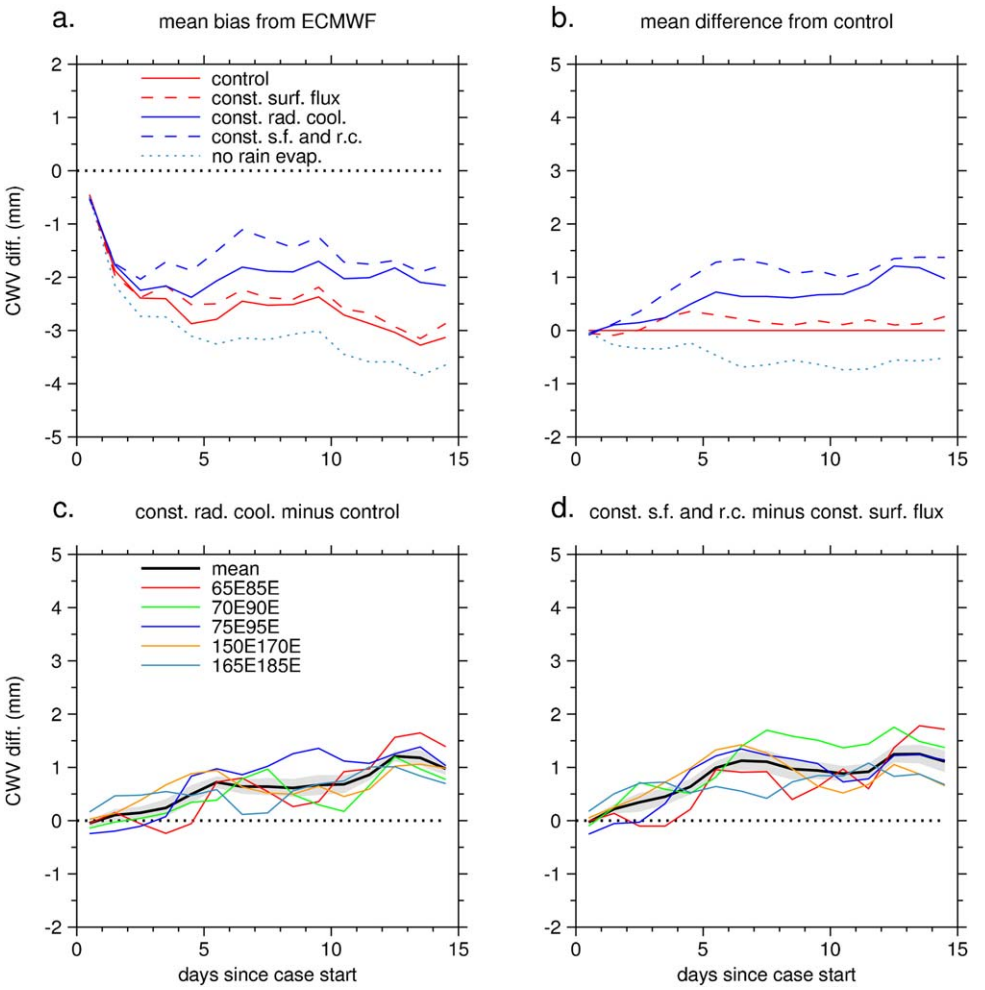

Figure 8. (a) Average CWV bias from ECMWF for each experiment over all five cases, (b) CWV difference for each experiment from control averaged over all five cases, (c) CWV constant radiative cooling experiment minus control for each case (colors) and for the mean (black line) with gray shading showing ±1 standard error of the mean, (d) as in Figure 8c but for constant surface flux and radiative cooling experiment minus constant surface flux experiment.

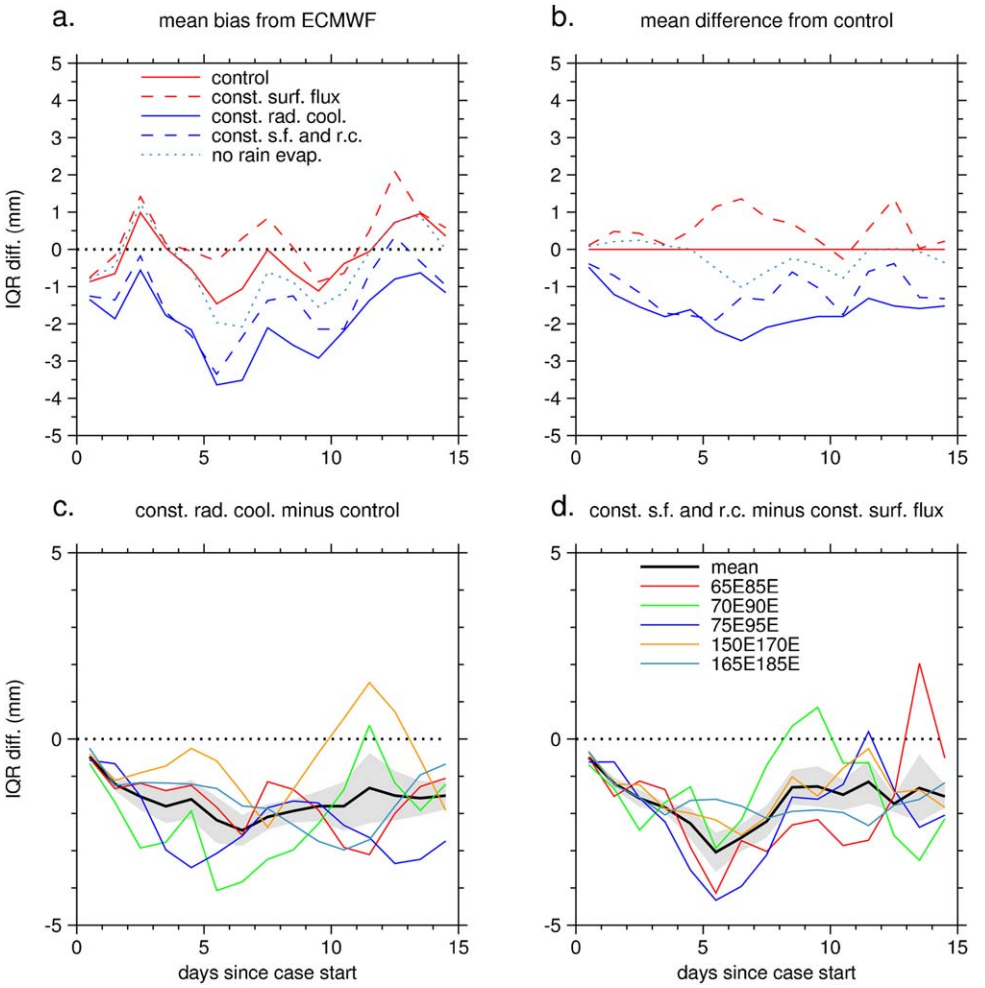

Figure 9. (a) Average CWV IQR bias from ECMWF for each experiment over all five cases, (b) CWV IQR difference for each experiment from control averaged over all five cases, (c) CWV IQR constant radiative cooling experiment minus control for each case (colors) and for the mean (black line) with gray shading showing ±1 standard error, (d) as in Figure 9c but for constant surface flux and radiative cooling experiment minus constant surface flux experiment.

simulations in HW16, albeit of smaller magnitude. For instance, for simulations with homogeneous initial conditions, the mean CWV in equilibrium is about 6 mm larger in the run with constant radiative cooling compared to the control run (HW16, their Figure 9a); for the run with constant radiative cooling initialized with an aggregated state taken from the end of the control run, the final state is also about 6 mm larger than the initial state (HW16, their Figure 12a). An argument attributing the smaller magnitude of these differences in the present study to the equalizing influence of advection/nudging from the lateral boundary conditions is presented below in section 6.4.

To isolate the effect of constant radiative cooling alone and the variability of this effect among the different cases, Figure 8c shows the differences between the constant radiative cooling run and the control run for each case (colored lines) while Figure 8d shows the differences between the run with constant radiative cooling and surface fluxes and the run with constant surface fluxes only for each case. The black lines are the means of all five cases, and the gray shading shows ±1 standard error of the mean. Overall, there is significant variation between different cases but there is a clear positive difference in both panels of approximately 1 mm by the end of the period. Note that, here and throughout this paper, the effects of suppressed rain evaporation and constant surface fluxes on mean state and aggregation metrics are generally not broken down into individual cases; this is because these effects are not as strong for mature convection in the idealized cases in HW16, and because the results in the present study are not as robust among different metrics.

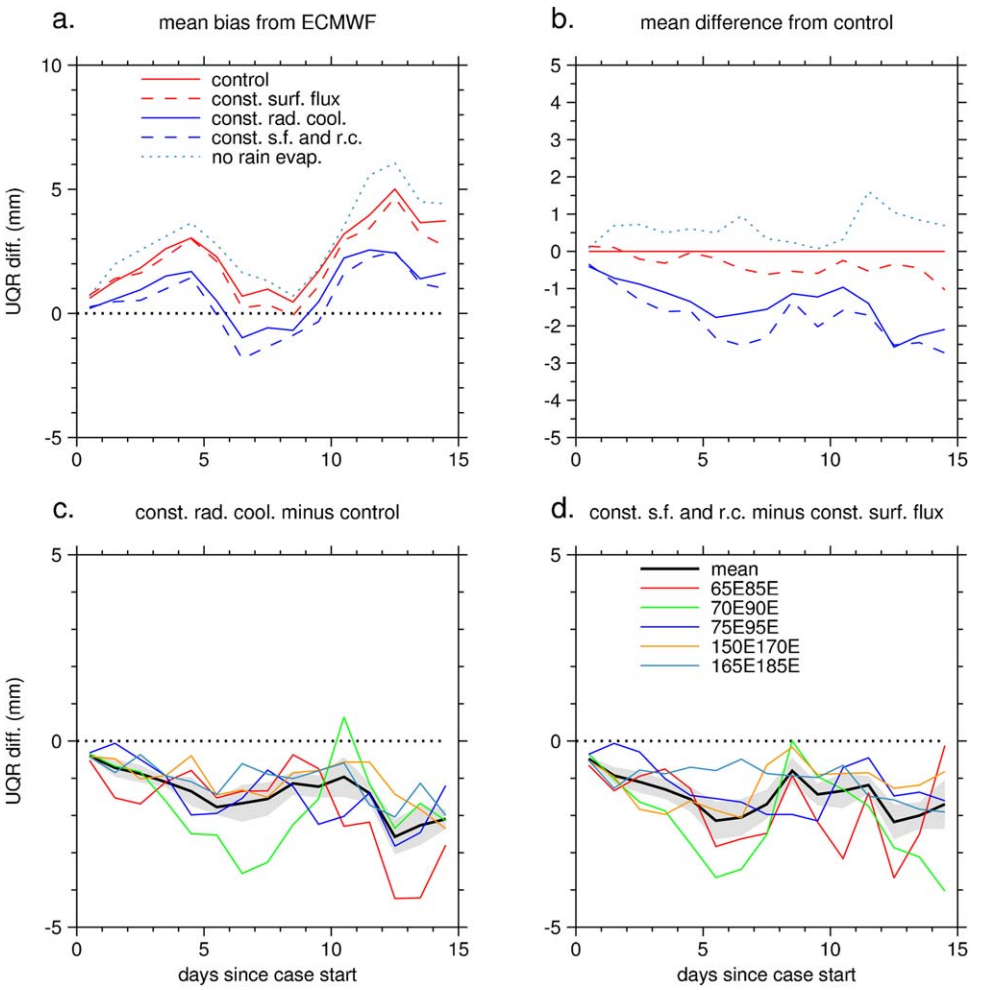

Figure 10. (a) Average CWV UQR bias from ECMWF for each experiment over all five cases, (b) CWV UQR difference for each experiment from control averaged over all five cases, (c) CWV UQR constant radiative cooling experiment minus control for each case (colors) and for the mean (black line) with gray shading showing ±1 standard error, (d) as in Figure 10c but for constant surface flux and radiative cooling experiment minus constant surface flux experiment.

Similar analysis to Figure 8, but for interquartile range (IQR) and "upper quantile range" (UQR) of CWV, are shown in Figures 9 and 10. Though there is somewhat more variability for these metrics among the different cases than for CWV (especially for IQR), the differences between the constant radiative cooling runs and their respective interactive radiation control runs for both metrics are down by between 1.5 and 2 mm on average by the end of the period (Figures 9c, 9d, 10c, and 10d). Again, these are small differences compared with the idealized models in HW16, but with the same sign.

The CWV autocorrelation length scale (Figures 11c and 11d) also shows a reduction on average for the constant radiative cooling runs, which again agrees with the idealized runs, and this reduction is even larger in the comparison between runs with constant surface fluxes. Constant surface fluxes alone seem to allow for slightly larger CWV autocorrelation length scales on average (Figures 11b, red dashed line), perhaps because there are no effective SST gradients to narrow convection zones, and it may be that this allows for a more significant loss of CWV organization when interactive radiation is turned off. Note that the apparent low bias for CWV autocorrelation length scale for all model experiments when compared to ECMWF (Figure 11a) may be partly related to higher resolution in the model runs.

Finally, Figure 12 does not show significant differences in SCAIP between model runs with and without interactive radiation effects. This does not agree with the findings above, which show decreased aggregation for runs without interactive radiation. However, it might be that precipitation features take longer to respond to the removal of radiative feedbacks than CWV-related aggregation metrics and that this time scale makes the effect

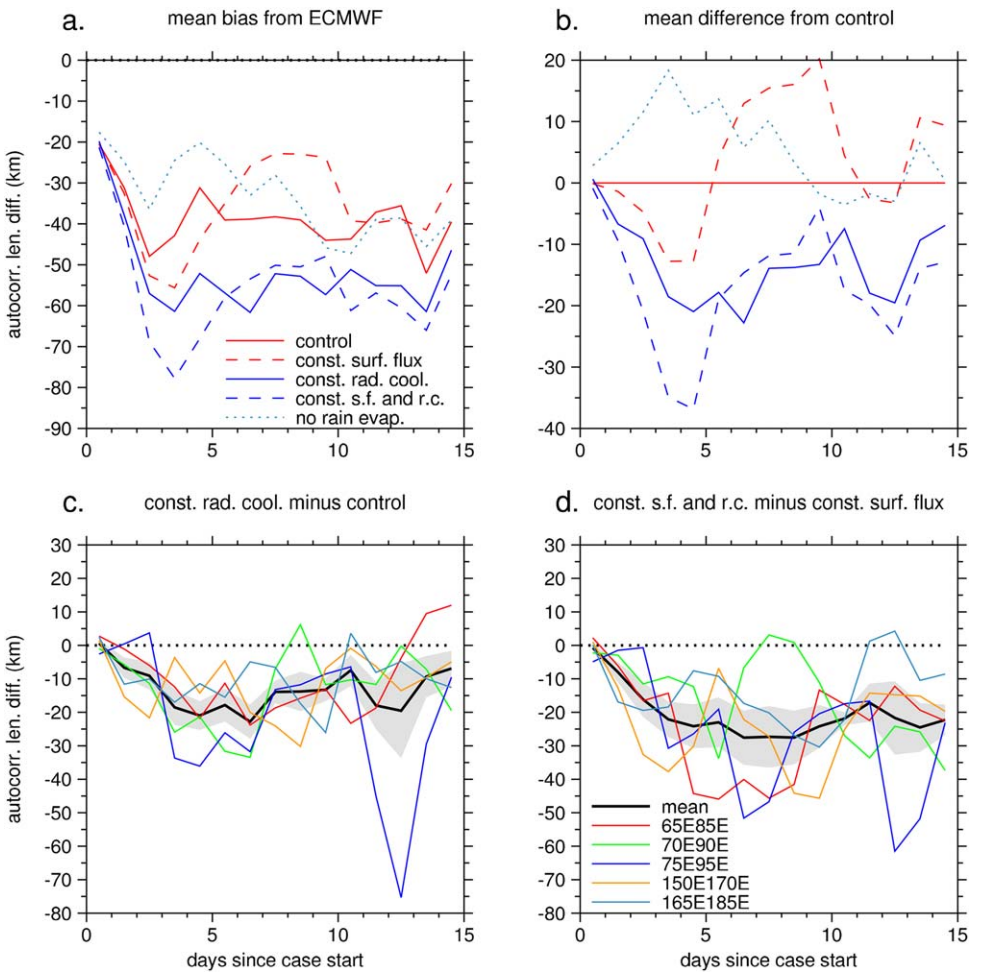

Figure 11. (a) Average CWV autocorrelation length scale bias from ECMWF for each experiment over all five cases, (b) CWV autocorrelation length scale difference for each experiment from control averaged over all five cases, (c) CWV autocorrelation length scale constant radiative cooling experiment minus control for each case (colors) and for the mean (black line) with gray shading showing ±1 standard error, (d) as in Figure 11c but for constant surface flux and radiative cooling experiment minus constant surface flux experiment.

difficult to observe here in light of the equalizing effects of advection from the lateral boundaries. SCAIP also exhibited a lot of variability in idealized runs discussed in HW16 (not shown) even after the system had reached a mature state. In observations analyzed in *Stein et al*. [2017], the area fraction of convective cores did not depend on the amount of organization (unlike anvil cloud amount, which was reduced for more aggregated states), so this may also mean that SCAIP is less sensitive to convective clustering than SCAI as measured from brightness temperature. Finally, as discussed below, constant radiative cooling runs have lower mean precipitation, and this could also result in lower SCAIP, for instance by reducing the number of heavy-rain regions; SCAI and SCAIP are not suitable indices for comparing states with significantly different domain-mean rainfall.

Figure 12 also shows an increase in SCAIP (decrease in organization) on average for constant surface flux runs, perhaps because of the effective lack of horizontal SST variability, although other aggregation metrics discussed above do not show strong surface flux effects. There is also significantly lower SCAIP (stronger organization) for runs with suppressed evaporation of rainfall, which agrees with the snapshot images in Figures 6 and 7. This behavior, in contrast to less robust rain evaporation effects on CWV aggregation metrics discussed above, may point to the relatively fast disruption of organized convection that rain-evaporation-driven cold pools can cause at the mesoscale [*Jeevanjee and Romps*, 2013], (although suppressing rain evaporation also affects latent heating profiles and the tropospheric moisture budget and reduces downdrafts in general, so there may be other causes of these differences besides cold pools). While this argument goes against traditional ideas about cold pools leading to organized features such as squall lines, these may be less important for the types of organization present in these cases.

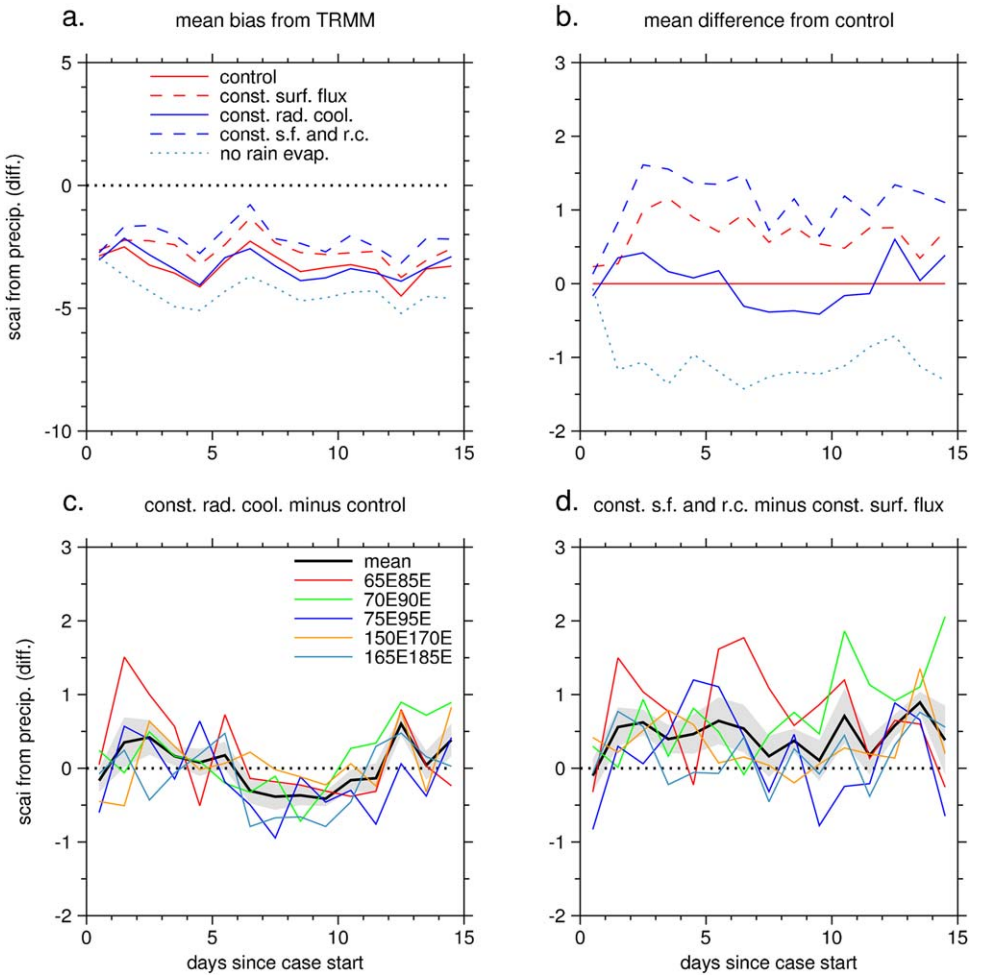

Figure 12. (a) Average SCAIP bias from TRMM for each experiment over all five cases, (b) SCAIP difference for each experiment from control averaged over all five cases, (c) SCAIP constant radiative cooling experiment minus control for each case (colors) and for the mean (black line) with gray shading showing ±1 standard error, (d) as in Figure 12c but for constant surface flux and radiative cooling experiment minus constant surface flux experiment.

It is important to note, as briefly mentioned above, that the mean precipitation (part of the "large-scale forcing" that is mostly constant in idealized runs or in observational studies such as *Tobin et al*. [2012]) can vary in these experiments. Figure 13 shows that the runs with constant radiative cooling actually have lower mean precipitation than the corresponding runs with interactive radiation. *Tobin et al*. [2012] find that, for a given state of aggregation, larger mean precipitation is associated with larger, not smaller, mean CWV, and this agrees with previous observational work showing a general positive correlation between CWV and precipitation [e.g., *Bretherton et al*., 2004; *Peters and Neelin*, 2006; *Holloway and Neelin*, 2009], so the precipitation effects seen in Figure 13 would, if anything, partly counteract the effects in mean CWV related to possible aggregation effects. Also, the temporal evolution of the precipitation difference is fast and at least as strong in the first half of the time period as the second half, unlike the CWV effects seen in Figure 8.

6.3. Distributions of CWV and Rainfall

As suggested by the systematic changes in both mean CWV and CWV IQR and UQR, CWV distributions change systematically in the different experiments. Figure 14a shows the mean probability density functions (PDFs) across the five cases for each experiment (for all sea and land points, though land fractions are very small). The control runs (shown for each case in Figure 14b) have fairly broad shapes around the peaks, and the two westernmost cases (with the lowest mean CWV) look bi-modal with secondary peaks around 30 mm. The differences in PDF between the constant radiative cooling runs and their respective interactive radiation runs are shown in Figures 14c and 14d; they confirm that constant radiative cooling leads to fewer

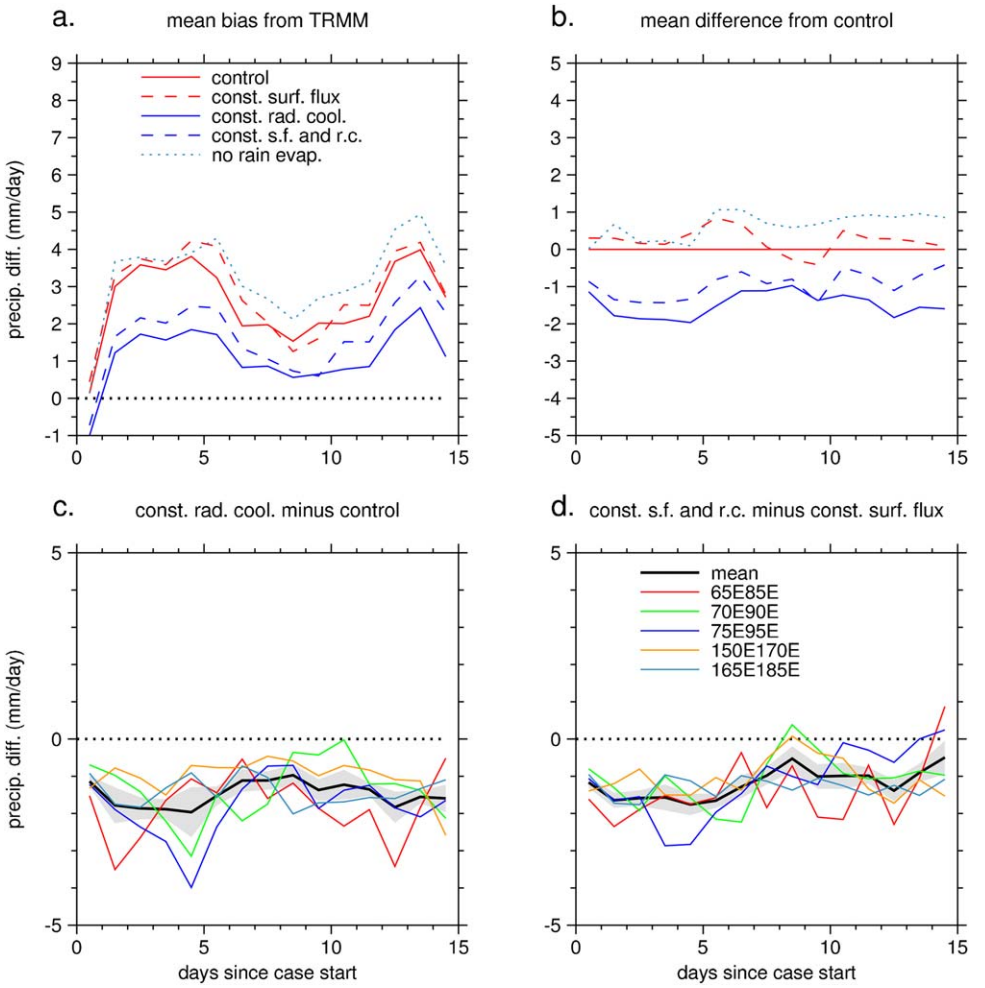

Figure 13. (a) Average precipitation bias from TRMM for each experiment over all five cases, (b) precipitation difference for each experiment from control averaged over all five cases, (c) precipitation constant radiative cooling experiment minus control for each case (colors) and for the mean (black line) with gray shading showing ±1 standard error of the mean, (d) as in Figure 13c but for constant surface flux and radiative cooling experiment minus constant surface flux experiment.

extremely dry regions or extremely moist regions and more of the typically moist regions near the peak of the distributions. The constant surface flux runs, meanwhile, have slightly larger counts in the dry tails than their respective interactive surface flux runs (probably due to the lack of a negative surface-flux feedback for very dry CWV regions, as seen earlier in Figure 3) but tend to have a shift in the peak toward higher CWV values (Figures 14e and 14f). This may be due to somewhat higher surface fluxes in and around the convective regions compared with the interactive surface flux runs.

The rainfall PDFs (not shown) look very similar for the different experiments among the different cases. However, there is a 25% decrease in the absolute counts of values with high rainrates (10–100 mm h^{-1}) for the two runs with constant radiative cooling relative to their respective interactive radiation experiments. There is a similar *increase* in these counts for the two runs with constant surface fluxes relative to their respective interactive surface flux experiments. Possible reasons for these differences are (1) interactive radiation may enhance convective organization and upward motion in cloudy regions and (2) interactive surface fluxes seem to reduce CWV in moister regions.

6.4. Reconciling Advection From Lateral Boundaries

The differences in mean CWV, IQR, and other measurements of the mean state and aggregation between different experiments are systematic but smaller than those in idealized experiments in HW16. Here I present a possible explanation for this based on the equalizing influence advection across the lateral boundaries.

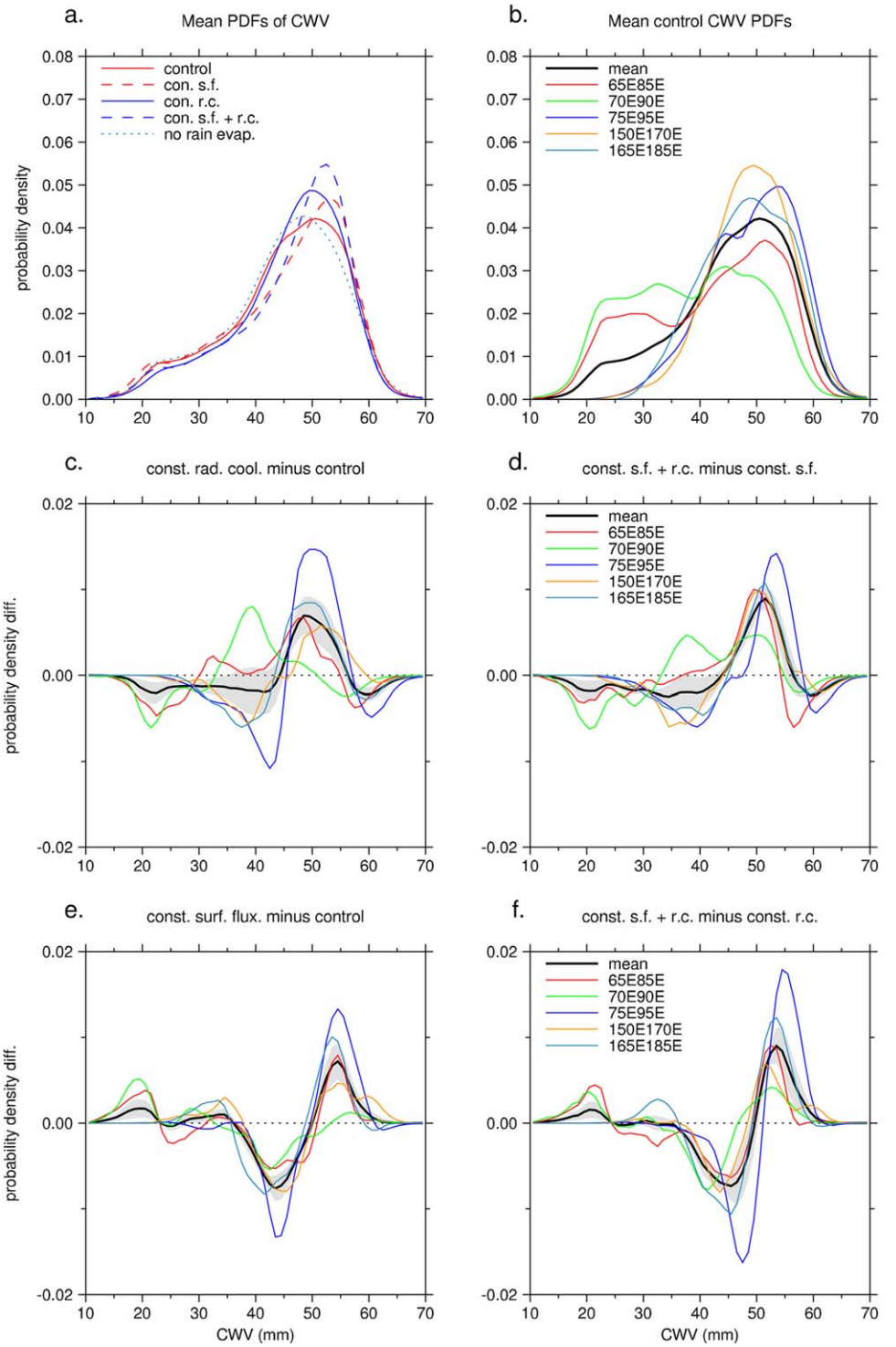

Figure 14. (a) Mean CWV probability density function (PDF within 10–70 mm CWV, in mm^{-1}) for each experiment over all five cases, (b) mean CWV PDF for the control run of each case and the mean over all control runs, (c) difference between PDF of constant radiative cooling run and control run for each case and mean, (d) difference between constant radiative cooling and constant surface flux run and control run, (e) difference between PDF of constant surface flux run and control run for each case and mean, and (f) difference between constant radiative cooling and constant surface flux run and constant surface flux run.

As mentioned in section 3, the lateral boundary conditions are taken from 12 km simulations which are themselves nested in ECMWF operational analyses. These lateral boundary conditions are the same for all experiments for a given case, and so they have the effect of eroding potential differences between the

different experiments. This effect is separate from, or in addition to, any real physical interaction between aggregation and large-scale circulations, and is due to the necessary limitations of the experimental design.

One way to think about these boundary effects and try to account for them is to estimate the amount of time it would take to replace the entire domain of a simulation with advection. Since humidity variance in the lower free troposphere explains a large part of CWV variance in the tropics [*Holloway and Neelin*, 2009], the total 850 hPa wind speed can be used to represent the movement of moist and dry CWV regions. I will use a single representative 850 hPa wind speed of 5 m s^{-1} (the domain-time-mean 850 hPa wind speed ranges from 4.6 to 5.9 m s^{-1} for the five control runs, with a standard deviations of around 3 m s^{-1} for the hourly speeds at each grid point for each case, and experiment runs are similar). Assuming this wind speed, for a 20° × 20° box it would take about 5 days to replace all the air in the domain assuming that horizontal low-level wind in any direction acts to transport air out of this level of the domain by either moving air out through the lateral boundaries or moving it to convective updrafts that transport it to upper levels (it is also assumed that subsiding air within the domain "replaces" low-level air equivalently in all runs). If I make an additional assumption that the constant radiative cooling runs have reached a rough equilibrium in their difference from their respective interactive radiation runs by the end of the case time period, then

$$r_{\mathrm{norad}} = -r_{\mathrm{adv}} = \frac{\Delta\phi}{\tau_{\mathrm{adv}}}, \tag{3}$$

where ϕ is some quantity (e.g., CWV or IQR), $\Delta\phi$ is ϕ of an experiment with fixed prescribed radiative cooling minus ϕ of the corresponding interactive radiation run at the assumed equilibrium time, r_{norad} is the effective rate of change of $\Delta\phi$ due to the removal of interactive radiation in the experiment run, r_{adv} is the effective rate of change of $\Delta\phi$ due to the equalizing effects of advection through the lateral boundaries, and τ_{adv} is the time scale for all of the low-level air in the domain to be replaced by air from outside of the domain (where τ_{adv} depends on wind speed and domain size as discussed above). The second relationship in the equation relies on the fact that replacing all of the air in the domain with air outside the domain for both model runs would result in zero $\Delta\phi$ if there were no effect from the radiation differences. Note that this is not a budget with sources or sinks but rather a statement of balance between a process of differentiation and one of equalization.

Table 2 compares r_{norad} estimates for four aggregation-related parameters using equation (3) with estimates of the total rate of change of the same parameters averaged over the first 10 days of idealized simulations from HW16 with fixed constant radiative cooling initialized with an aggregated state (see HW16, their Figure 12). The r_{norad} estimates from the runs in the present study are made assuming a τ_{adv} of 5 days and evaluating $\Delta\phi$ using an approximate value taken from the averages over the final days of analyses shown in Figures 8c, 8d, 9c, and 9d. The r_{norad} values from the present study are the same order of magnitude as the respective HW16 idealized model disaggregation rates, with the rate magnitudes in the present study being 2–3 times smaller than in HW16 for mean CWV and UQR but slightly larger for IQR and CWV autocorrelation length scale. Given the uncertainties in the estimates of r_{norad} and their contingency on several broad assumptions, these values are comparable to each other. They do not contradict the hypothesis that the changes in aggregation metrics due to the absence of interactive radiation in the realistic runs in the present study have the same causes, and have similar rates, as the changes in disaggregation from the runs in HW16.

On the other hand, this analysis does not prove that the mechanisms are the same as in the idealized cases. And for that matter, the exact mechanisms are not certain for either idealized or realistic cases (though section 6.5 below looks at this in more detail). The fact that SCAIP does not show systematic changes due to the absence of interactive radiation adds further doubt, although it is possible that the magnitude of the changes to CWV organization are not large enough to measure systematic changes in precipitation organization. Nevertheless, the systematic differences suggest a link.

Table 2. Estimates of Rate of Change of Aggregation-Related Metrics Due to Absence of Interactive Radiation in the Five Cases From Equation (3) Using a τ_{adv} of 5 Days, and Corresponding Rate of Change (Averaged Over First 10 Days) in Idealized Runs From HW16 With Fixed Constant Radiative Cooling Initialized With an Aggregated State

Metric (and Rate Units)	r_{norad}	HW16
CWV (mm d^{-1})	0.2	0.5
IQR (mm d^{-1})	−0.3	−0.2
UQR (mm d^{-1})	−0.4	−1.3
Autocorr. Len. (km d^{-1})	−2.0	−1.5

For the mechanism-denial tests other than those for interactive radiation, results are less clear. An

Table 3. Differences in MSE Spatial Variance Budget Terms Between Mechanism-Denial Experiments and Their Respective Full-Mechanism Controls[a]

Experiment Difference	Tot. Diab.	Conv.	Sum
Const. rad. cool. minus control	-3.25 ± 0.29	3.07 ± 0.29	-0.17 ± 0.03
Const. s.f. and r.c. minus const. surf. flux	-4.22 ± 0.65	4.06 ± 0.69	-0.16 ± 0.09
Const. surf. flux minus control	2.53 ± 0.91	-2.45 ± 0.95	0.08 ± 0.08
Const. s.f. and r.c. minus const. rad. cool.	1.56 ± 0.45	-1.46 ± 0.47	0.09 ± 0.04
No rain evap. minus control	0.30 ± 0.12	-0.31 ± 0.12	-0.00 ± 0.03

[a]Terms shown are the total diabatic heating, the convergence term, and the sum of these two which equals one half of the net rate of change of $\{\hat{h}'^2\}$ over the period (see equation (2)). For each term, the mean of all five time-mean case values is shown, with the standard error of the mean of those five values shown after the "±," in 10^{13} J^2 m^{-4} d^{-1}.

analogous $\Delta\phi$ for the suppression of interactive surface fluxes is small or inconsistent among the different cases in the present study for the aggregation metrics, and HW16 and other studies of idealized self-aggregation suggest that interactive surface fluxes are not necessary for the maintenance of an already aggregated state [*Wing et al.*, 2017]. The effects of suppressing rain evaporation on the organization of CWV and precipitation are intriguing, but they are also less certain in HW16 (regarding aggregation at more mature stages for runs with interactive radiation).

6.5. MSE Variance Budget Analysis

The changes in some of the MSE spatial variance budget terms for the mechanism-denial experiments as compared with their respective full-mechanism control experiments are shown in Table 3. The first two rows show the effects of the absence of interactive radiation. In both comparisons, the large reduction in the total diabatic heating term is mostly offset by an increase in the convergence term; the actual convergence term is positive in four of the constant radiative cooling run, while it is negative in all the control runs. Part of this near-compensation of terms is likely related to the restoring effects of the lateral boundary conditions discussed in section 6.4 above. Note that the constant radiative cooling run (row 1 of Table 3) has somewhat larger surface fluxes than the control run, with a 0.795×10^{13} J^2 m^{-4} d^{-1} total difference (not shown), but this is small compared to the total diabatic term difference. The net difference when all terms are summed is smaller than the first two terms shown, but it is consistently negative, confirming that the change in $\{\hat{h}'^2\}$ over the time period is smaller (more negative) than in the corresponding interactive-radiation runs. This agrees with the finding that aggregation is lower in the runs without interactive radiation.

The runs with constant surface fluxes (rows 3–4 of Table 3) have larger diabatic heating terms than the corresponding interactive-radiation runs, and again this is mostly compensated by much lower convergence terms. The radiation terms in the constant surface flux run (row 3 of Table 3) do not change much compared to the control run, with only a 0.176×10^{13} J^2 m^{-4} d^{-1} total radiation difference (not shown). There is a net positive change for the sum of the terms, which suggests, somewhat counterintuitively, that removing interactive surface fluxes actually increases aggregation; this does make sense, though, when looking at the negative surface flux terms in Figure 3.

The runs with suppressed evaporation of rainfall (row 5 of Table 3) have similar values as control for all terms in general, with slightly larger total diabatic terms (mainly from slightly larger surface flux terms) and correspondingly slightly smaller convergence terms. This leaves a negligible net difference, which agrees with the somewhat small or contradictory effects of suppressed rain evaporation on aggregation metrics seen in Figures 9–11. The stronger effects on precipitation organization, including SCAIP (Figure 12), are seemingly separate from the CWV organization, at least given the fairly rapid equalizing effects of lateral boundary advection. The significant reduction in mean CWV (Figure 8) and increase in mean precipitation (Figure 13) for the suppressed evaporation runs could plausibly be explained by the microphysics itself: less rain evaporating in the troposphere and therefore more rain reaching the ground.

7. Discussion and Conclusions

The initial hypothesis motivating the present study was that simulations of tropical convection with a realistic configuration would exhibit similar convective aggregation behavior, caused by similar mechanisms, as that seen in idealized configurations of the same model in HW16. To test this hypothesis, five 15 day cases over $10^\circ \times 10^\circ$ domains, including a control run and four mechanism-denial experiments for each case,

have been analyzed. For the control runs, the time-domain-mean terms of the MSE spatial variance budget are broadly consistent with the corresponding terms from the control run in HW16 in the latter half of the period when the convection has aggregated, although the surface flux term in the present study is even more negative for the two cases with the largest regions of low-CWV air, and the longwave terms in the present study are larger in magnitude relative to the shortwave terms. Analysis of the distribution of the terms across regions with different CRH shows the importance of positive longwave feedback in the moistest regions, as well as consistent strong negative surface flux feedback in the driest regions, consistent with HW16. These findings are consistent with the idea that organized convection is maintained by similar mechanisms to those in idealized RCE simulations.

The overall pattern of moist and dry regions is similar across the control runs and experiments for each case, but this is largely expected given the imposed lateral boundary conditions shared across experiments. The aggregation metrics used in HW16 (mean CWV, CWV IQR, CWV UQR, CWV autocorrelation length scale, and $\{\hat{h}'^2\}$) all show systematic differences in the runs with constant radiative cooling with respect to their corresponding control runs with interactive radiation, and these differences are consistent with those seen in idealized runs in HW16. While the magnitude of these differences is generally smaller than that seen between the aggregated state and disaggregated state in HW16 (even in the simulation initialized with an aggregated state with constant radiative cooling), the implied rate of change estimated by assuming an equilibrium between disaggregation by the absence of interactive radiation and aggregation by the replacement of air within the domain by air from outside the domain through the lateral boundary conditions is broadly consistent with the rates of change in the HW16 simulation initialized with an aggregated state and run with constant radiative cooling. These findings are consistent with the hypothesis above as well.

The null hypothesis that there is no systematic relationship between mechanisms for convective aggregation in idealized simulations and realistic simulations is largely inconsistent with the evidence presented above. However, the organization of precipitation clusters, as measured by SCAIP, does not vary systematically between the runs with and without interactive radiation, casting some doubt on the main hypothesis. A plausible explanation is that the relatively small changes in CWV-related aggregation metrics that are seen at the end of the constant radiative cooling runs are not large enough to allow for significant changes in precipitation organization. Indeed, even in the idealized runs discussed in HW16, there can be quite a bit of variability in SCAIP when there is either a mature aggregated or disaggregated state as measured by CWV-related aggregation metrics (not shown), so this is a rather noisy metric. The rainfall, once clustered, may also have some additional hysteresis, meaning it resists disaggregation more strongly than the CWV fields.

There is considerable uncertainty in the arguments presented above, particularly in terms of the estimate of the rate of disaggregation by the absence of interactive radiation. One way to test the validity of this estimation would be to do a range of simulations with different domain sizes, since the equalizing effect of advection from the lateral boundary conditions should get smaller with increasing domain size. There is also the possibility that the mechanisms found in the idealized simulations in HW16 were due to model artifacts which also act in the realistic simulations in the present study. However, the systematic differences in simulations with and without interactive radiation suggest the importance of radiation feedbacks in helping to maintain and amplify organized tropical convection, as also found in recent studies of global-scale idealized simulations with Earth-like rotation [*Arnold and Randall*, 2015; *Bretherton and Khairoutdinov*, 2015]. The present study suggests that findings from those studies could plausibly apply to real-world convective organization. If so, it would be good to further explore observational approaches to addressing aggregation questions as well as further numerical simulations with model configurations spanning a range of complexity.

Acknowledgments

I thank Thorwald Stein for extensive comments on an earlier draft of this paper. Paul Field provided moisture conservation code for the limited-area version of the MetUM. Grenville Lister provided assistance with running the model. Adrian Lock and Rob Warren helped with advice for modifying the MetUM code for mechanism-denial experiments. This work made use of the facilities of HECToR (and its successor, ARCHER), the UK's national high-performance computing service, which is provided by UoE HPCx Ltd. at the University of Edinburgh, Cray Inc. and NAG Ltd., and funded by the Office of Science and Technology through EPSRC's High End Computing Program. I was funded from UK NERC grant NE/I021012/1 for the first part of this study. The MetUM simulation data will be made available through the NERC Centre for Environmental Data Archival (CEDA) at catalogue.ceda.ac.uk: in the meantime, the data can be made available by the author on request.

References

Arnold, N. P., and D. A. Randall (2015), Global-scale convective aggregation: Implications for the Madden-Julian Oscillation, *J. Adv. Model. Earth Syst.*, *7*, 1499–1518, doi:10.1002/2015MS000498.

Bretherton, C. S., and M. F. Khairoutdinov (2015), Convective self-aggregation feedbacks in near-global cloud-resolving simulations of an aquaplanet, *J. Adv. Model. Earth Syst.*, *7*, 1765–1787, doi:10.1002/2015MS000499.

Bretherton, C. S., M. E. Peters, and L. E. Back (2004), Relationships between water vapor path and precipitation over the tropical oceans, *J. Clim.*, *17*, 1517–1528.

Bretherton, C. S., P. N. Blossey, and M. Khairoutdinov (2005), An energy-balance analysis of deep convective self-aggregation above uniform SST, *J. Atmos. Sci.*, *62*, 4273–4292.

Coppin, D., and S. Bony (2015), Physical mechanisms controlling the initiation of convective self-aggregation in a General Circulation Model, *J. Adv. Model. Earth Syst.*, *7*, 2060–2078, doi:10.1002/2015MS000571.

Davies, T., M. J. P. Cullen, A. J. Malcolm, M. H. Mawson, A. Staniforth, A. A. White, and N. Wood (2005), A new dynamical core for the Met Office's global and regional modelling of the atmosphere, *Q. J. R. Meteorol. Soc.*, *131*(608), 1759–1782.

Hohenegger, C., and B. Stevens (2016), Coupled radiative convective equilibrium simulations with explicit and parameterized convection, *J. Adv. Model. Earth Syst.*, *8*, 1468–1482, doi:10.1002/2016MS000666.

Holloway, C. E., and J. D. Neelin (2009), Moisture vertical structure, column water vapor, and tropical deep convection, *J. Atmos. Sci.*, *66*, 1665–1683.

Holloway, C. E., and S. J. Woolnough (2016), The sensitivity of convective aggregation to diabatic processes in idealized radiative-convective equilibrium simulations, *J. Adv. Model. Earth Syst.*, *8*, 166–195, doi:10.1002/2015MS000511.

Holloway, C. E., S. J. Woolnough, and G. M. S. Lister (2012), Precipitation distributions for explicit versus parametrized convection in a large-domain high-resolution tropical case study, *Q. J. Roy. Meteor. Soc.*, *138*, 1692–1708.

Holloway, C. E., S. J. Woolnough, and G. M. S. Lister (2013), The effects of explicit versus parameterized convection on the MJO in a large-domain high-resolution tropical case study. Part I: Characterization of large-scale organization and propagation, *J. Atmos. Sci.*, *70*(5), 1342–1369, doi:10.1175/JAS-D-12-0227.1.

Holloway, C. E., S. J. Woolnough, and G. M. S. Lister (2015), The effects of explicit versus parameterized convection on the MJO in a large-domain high-resolution tropical case study. Part II: Processes leading to differences in MJO development, *J. Atmos. Sci.*, *72*(7), 2719–2743, doi:10.1175/JAS-D-14-0308.1.

Huffman, G. J., R. F. Adler, D. T. Bolvin, G. J. Gu, E. J. Nelkin, K. P. Bowman, Y. Hoong, E. F. Stocker, and D. B. Wolff (2007), The TRMM Multisatellite Precipitation Analysis (TMPA): Quasi-global, multiyear, combined-sensor precipitation estimates at fine scales, *J. Hydrometeorol.*, *78*, 2179–2196.

Jeevanjee, N., and D. M. Romps (2013), Convective self-aggregation, cold pools, and domain size, *Geophys. Res. Lett.*, *40*, 994–998, doi:10.1002/grl.50204.

Lean, H. W., P. A. Clark, M. Dixon, N. M. Roberts, A. Fitch, R. Forbes, and C. Halliwell (2008), Characteristics of high-resolution versions of the Met Office Unified Model for forecasting convection over the United Kingdom, *Mon. Weather Rev.*, *136*, 3408–3424.

Muller, C., and S. Bony (2015), What favors convective aggregation and why?, *Geophys. Res. Lett.*, *42*, 5626–5634, doi:10.1002/2015GL064260.

Muller, C. J., and I. M. Held (2012), Detailed investigation of the self-aggregation of convection in cloud-resolving simulations, *J. Atmos. Sci.*, *69*(8), 2551–2565, doi:10.1175/JAS-D-11-0257.1.

Nolan, D. S., E. D. Rappin, and K. A. Emanuel (2007), Tropical cyclogenesis sensitivity to environmental parameters in radiative-convective equilibrium, *Q. J. R. Meteorol. Soc.*, *133*, 2085–2107.

Peters, O., and J. D. Neelin (2006), Critical phenomena in atmospheric precipitation, *Nat. Phys.*, *2*, 393–396.

Reed, K. A., B. Medeiros, J. T. Bacmeister, and P. H. Lauritzen (2015), Global radiative–convective equilibrium in the Community Atmosphere Model, version 5, *J. Atmos. Sci.*, *72*(5), 2183–2197, doi:10.1175/JAS-D-14-0268.1.

Roberts, N. M. (2003), The impact of a change to the use of the convection scheme to high-resolution simulations of convective events, *Tech. Rep. 407*, 30 pp., UK Met Off, Exeter, U. K.

Stein, T. H. M., C. E. Holloway, I. Tobin, and S. Bony (2017), Observed relationships between cloud vertical structure and convective aggregation over tropical ocean, *J. Clim.*, *30*(6), 2187–2207, doi:10.1175/JCLI-D-16-0125.1.

Tobin, I., S. Bony, and R. Roca (2012), Observational evidence for relationships between the degree of aggregation of deep convection, water vapor, surface fluxes, and radiation, *J. Clim.*, *25*(20), 6885–6904, doi:10.1175/JCLI-D-11-00258.1.

Tobin, I., S. Bony, C. E. Holloway, J.-Y. Grandpeix, G. Sèze, D. Coppin, S. J. Woolnough, and R. Roca (2013), Does convective aggregation need to be represented in cumulus parameterizations?, *J. Adv. Model. Earth Syst.*, *5*(4), 692–703, doi:10.1002/jame.20047.

Tompkins, A. M. (2001), Organization of tropical convection in low vertical wind shears: The role of water vapor, *J. Atmos. Sci.*, *58*, 529–545.

Waliser, D. E., et al. (2012), The "year" of tropical convection (May 2008-April 2010): Climate variability and weather highlights, *Bull. Am. Meteorol. Soc.*, *93*, 1189–1218.

Wilson, D. R., and S. P. Ballard (1999), A microphysically based precipitation scheme for the UK Meteorological Office Unified Model, *Q. J. R. Meteorol. Soc.*, *125*, 1607–1636.

Wing, A. A., and K. A. Emanuel (2014), Physical mechanisms controlling self-aggregation of convection in idealized numerical modeling simulations, *J. Adv. Model. Earth Syst.*, *6*(1), 59–74, doi:10.1002/2013MS000269.

Wing, A. A., and T. W. Cronin (2016), Self-aggregation of convection in long channel geometry, *Q. J. R. Meteorol. Soc.*, *142*, 1–15, doi:10.1002/qj.2628.

Wing, A. A., S. J. Camargo, and A. H. Sobel (2016), Role of radiative–convective feedbacks in spontaneous tropical cyclogenesis in idealized numerical simulations, *J. Atmos. Sci.*, *73*(7), 2633–2642, doi:10.1175/JAS-D-15-0380.1.

Wing, A. A., K. Emanuel, C. E. Holloway, and C. Muller (2017), Convective self-aggregation in numerical simulations: A review, *Surv. Geophys.*, doi:10.1007/s10712-017-9408-4.